

Characteristics of Femtosecond Laser Induced Filament and Energy Coupling by Nanosecond Laser Pulse in Air

S. Pokharel¹ and A. A. Tropina¹

Department of Aerospace Engineering, Texas A&M University, TX 77843

(*Electronic mail: pokharel_sagar@tamu.edu)

(Dated: February 4, 2025)

This study presents a detailed plasma kinetics model for laser-induced non-equilibrium plasmas in atmospheric pressure air, incorporating a self-consistent energy balance and refined rate expressions within a three-temperature framework. The model is validated against experimental data of femtosecond-laser-induced filaments, showing good agreement in electron dynamics and gas temperature. The analysis focuses on femtosecond filament decay kinetics and characteristic properties across varying initial electron densities and electron temperatures, including cases with oxygen addition and its influence on decay behavior. The study further examines energy coupling between the femtosecond filament and nanosecond laser pulse, identifying dominant kinetic pathways and optimal time delays through a comparative analysis of single-pulse and dual-pulse plasmas. Additionally, results indicate that temporal shaping of the nanosecond laser pulse intensity enhances dual-pulse performance relative to Gaussian pulses.

I. INTRODUCTION

Laser energy deposition and laser generated plasmas have numerous potential applications, such as aerodynamic flow control¹, fuel-air mixture ignition², flame stabilization³, directed energy deposition⁴, hazardous gas tracing⁵, machining and fabrication for modern semiconductors⁶, waveguiding⁷, laser diagnostics⁸, etc. Depending on the characteristics of the plasma kernel, e.g., electron number density, electron energy, size, shape, translational and vibrational temperatures, and pressure, different flow dynamics are observed at hydrodynamic time scales $t > 1\mu s$. For efficient development of applications based on the controlled laser energy deposition, a detailed understanding of plasma kinetics, hydrodynamics, and associated aero-optical effects is required.

The exponential nature of plasma buildup while using nanosecond (ns) laser pulses often results in uncontrolled energy deposition. To address this, a dual-pulse approach, incorporating both ns-ns and femtosecond (fs)-ns configurations, has been proposed^{1,9,10}. This method enables the decoupling of initial ionization and seeded electron generation by the first pulse from the subsequent energy deposition, allowing for greater control over plasma formation. The energy addition by the second heating pulse^{5,11,12}. Dual-laser pulse setups, particularly those incorporating fs filaments, are being explored for controlled plasma generation and energy deposition. Fs filaments are characterized by high-intensity pre-ionization and self-focusing, and facilitate long-distance propagation and waveguiding of subsequent laser pulses. These systems, enhanced by additional energy sources, enable rapid triggering of pulsed discharges and advanced diagnostics for low-temperature plasmas and ignition. The efficiency of energy deposition in optimal pulse pairings is influenced by the interaction between the second laser pulse and the initial plasma kernel. Thus, a comprehensive characterization of fs filaments at atmospheric pressure, along with their coupling with ns laser pulses, is crucial for applications in aerospace and other advanced technological fields.

The properties of laser-induced plasmas in ambient air

vary significantly due to factors such as laser pulse energy, system jitter, focusing configurations, humidity, and inhomogeneities caused by particulates. While existing studies have mainly focused on initial electron density using interferometry¹³⁻¹⁵, plasma kinetics and other properties under highly non-equilibrium conditions remain under-explored. Experimental techniques face challenges caused by fast time scales and small filament dimensions. Recent experimental investigations have utilized techniques such as Thomson scattering¹⁶, microwave scattering^{17,18}, and optical emission spectroscopy¹⁹ for more comprehensive studies of femtosecond-laser-induced filament dynamics. However, studies on their coupling with nanosecond laser pulses^{1,5,17,20} remain limited.

Th  berge et al.²¹ demonstrated experimentally and numerically that the plasma density and diameter of the plasma column within the core of a single filament are strongly influenced by the focal length of the lens used to focus the beam, while being only minimally affected by the laser power. The electron density in femtosecond (fs)-laser induced filaments has been reported to range from $1.0 \times 10^{14} \text{ cm}^{-3}$ to $1.0 \times 10^{18} \text{ cm}^{-3}$, with free propagation resulting in the lowest densities and tighter focusing optics yielding higher densities^{21,22}. For extremely tight focusing, where the numerical aperture (NA) exceeds 0.08, plasma densities up to $1.0 \times 10^{19} \text{ cm}^{-3}$ have been observed^{23,24}. Braun et al.²⁵ demonstrated the self-channeling property of fs laser filaments in air over distances exceeding 20 m. More recent studies with chirped pulses reported propagation distances up to 1 km, retaining 80% of the initial pulse energy²⁶.

Quantitative measurements of the temporal evolution of plasma properties in fs laser-induced (FLI) filaments have been reported, including gas temperature⁸, vibrational temperature²⁷, and electron density^{13-15,18}. Two-dimensional filament properties in argon have been studied by Bak²⁸. Recent work utilizing Thomson scattering has experimentally measured electron density, electron temperature, gas temperature, and gas density²⁹ on the same filament. The influence of the ns-heating pulse on fs laser filaments has been explored in several studies. Papeer demonstrated the slowing down of

plasma decay with the heating pulse²⁰, while Polynkin observed the appearance of so-called plasma bullets with the energy addition from the ns-heating pulse³⁰. Limbach investigated the absorption of a second pulse beyond breakdown conditions by adding a high energy ns pulse¹. Energy addition to fs-filaments, which causes triggering of air-gap discharge³¹ and combined fs and microwave discharges³² were also studied.

Studies related to the fs laser propagation in the media have explored various aspects of laser-induced plasma dynamics, including electron yield calculations and modeling filament conditions for varying power and focusing setups^{21,33}. In the most common approach the electron density is evaluated considering the clamping intensity of the laser, calculated from the balance of the photoionization yield³⁴ and the Kerr focusing, without considering the spatially expanding and contracting structure of the fs filament^{35,36}.

For plasma kinetics in laser-induced highly non-equilibrium plasmas, limited studies have validated electron dynamics and thermalization through the comparison with experimental measurements. Aleksandrov developed a reduced reaction scheme fitted to the measured plasma decay curves¹³. Papeer *et al.*¹⁸ employed a detailed plasma kinetics model to fit experimental decay curves and determine quantitative electron density values, but the specifics of the reaction scheme used were not clearly described. The re-energization capabilities required for modeling the coupling of a ns-heating pulse with a fs-filament are often neglected. Modeling plasma kinetics for decay alone is insufficient for dual-pulse laser plasma applications, as the kinetics of plasma decay and re-energization are significantly different³⁷. Shneider investigated the energy addition to fs-filaments in air using a dual laser pulse approach, incorporating detailed plasma kinetics³⁸. The drift-diffusion model has been effectively applied to describe laser plasma dynamics³⁶ in nitrogen, showing good agreement with experimental results. The development of plasma kinetics reaction scheme for non-equilibrium plasma in air often relies on the work of Kosy³⁹ and other contributions from the literature⁴⁰⁻⁴².

Accurate modeling of laser-induced plasma phenomena over extended timescales requires self-consistent approaches that integrate multi-species kinetics, energy exchange mechanisms across various energy modes, and dimensional considerations. Significant gaps remain in the characterization of fs-ns dual-laser pulse plasmas and the development of reliable plasma dynamics solvers with robust validation for such applications. Comprehensive models are required to accurately represent these phenomena, focusing on multi-laser interactions (e.g., dual-laser pulses) rather than solely capturing electron decay. Detailed plasma kinetics models are crucial for low-temperature, highly non-equilibrium plasmas below breakdown and subsequent laser-plasma interactions, as they must capture thermochemical non-equilibrium characteristics, plasma revival, and consistent energy thermalization.

This work focuses on the development of comprehensive plasma kinetics models for laser-induced plasmas in atmospheric pressure air, incorporating a self-consistent energy balance for non-equilibrium plasmas and improved rate ex-

pressions under a multi-temperature framework. Emphasis is placed on fs-filament dynamics and their coupling with ns laser pulses, addressing challenges in modeling filament behavior, comparing experimental results, and understanding interaction mechanisms. The study includes the development and validation of plasma kinetics models for $N_2 - O_2$ mixtures, followed by detailed investigations into fs-filament behavior, dual-pulse plasma interactions, and recent advances in coupling mechanisms and plasma dynamics.

II. MATHEMATICAL MODEL AND SOLVER DEVELOPMENT

The femtosecond laser-induced plasma channel is distinct from other plasma sources due to its pronounced thermochemical non-equilibrium characteristics. While some applications, such as ignition, aerodynamic flow control, and flow-field modification, rely on thermal effects, others, including sensitive optical diagnostics, precise energy deposition, the prevention of uncontrolled breakdown, and wave-guiding, operate within low-temperature, highly non-equilibrium plasma conditions, necessitating specialized models. Ignition can still be achieved with higher efficiency without realizing such high temperatures reached in thermal post-breakdown plasmas, but necessitates control over the energy deposition process.

In our previous work³⁶, we introduced a drift-diffusion-based fluid model for non-equilibrium plasmas, incorporating detailed chemical kinetics in multiple dimensions. Additionally, we developed a three-temperature plasma kinetic model coupled with a Navier-Stokes solver to accurately simulate the decay of laser induced plasma. The plasma solver, LOTASFOAM³⁶, utilizing OpenFOAM libraries⁴³, integrates a multi-temperature plasma model alongside a hybrid central solver for hydrodynamics with wide range of mach numbers. Addressing challenges associated with modeling the thermochemical non-equilibrium nature of laser-induced low-temperature plasma, we identified and resolved several key issues. Our approach focused on achieving a self-consistent balance of energy in plasma reactions, ensuring the inclusion of energy exchange between various energy modes within a reaction. This was crucial for maintaining a consistent energy balance in the plasma, especially over extended timescales, a feature currently lacking in multi-dimensional models. Additionally, our model incorporated appropriate considerations for charge transport involving negative ions and electrons, introducing a separate equation for the electric field. Furthermore, vibrational non-equilibrium was addressed by including a dedicated vibrational energy equation. These enhancements contribute significantly to a more comprehensive and accurate description of laser-induced low-temperature plasma behavior in multi-dimensional models, with extensive validation and robustness demonstrated for nitrogen plasmas at atmospheric pressure^{36,44,45}.

The plasma dynamics solver is part of a holistic framework that incorporates multi-physics details for studying laser-induced plasmas and their interactions across various applications. Although the presented results do not involve cou-

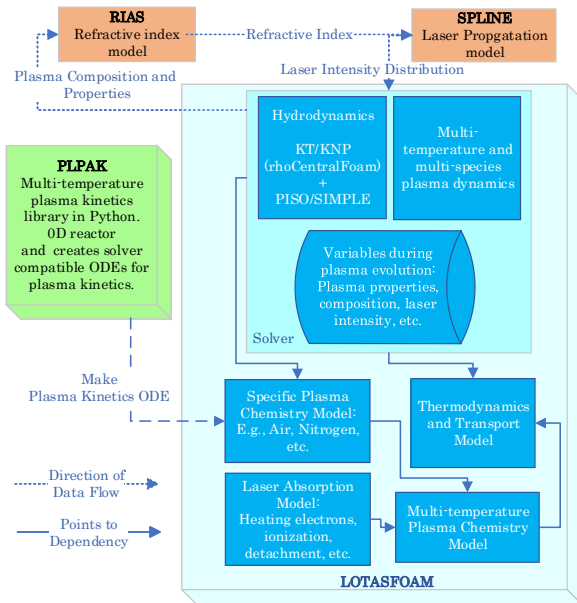


Figure 1. Schematic diagram for the multi-physics solver network.

pling between laser propagation and plasma dynamics, this framework integrates key components, including the SPLINE model for laser propagation, the PLPAK (Package for Low Temperature Plasma Kinetics) library for plasma kinetics development, and the RIAS module for refractive index and laser absorption calculations, all interfaced with the LOTASFOAM solver to form a comprehensive multi-physics solver suit. The schematic of this solver architecture is presented in Figure 1. The detailed mathematical model utilized is explained in a previous publication³⁶, while the extension and implementation of the plasma kinetics for air and additional details related to the coupling of laser-plasma interactions are presented herein.

A significant extension in this work is the development of self-consistent plasma kinetics models for air plasmas, facilitated by the PLPAK library. PLPAK is a standalone utility for developing 0D-3T (zero-dimensional and three-temperature) plasma kinetics models, enabling rapid testing and analysis of reaction mechanisms. It generates plasma-system ODEs for drift-diffusion solvers in major programming languages. The library incorporates BOLSIG+ rates, supports multi-temperature-dependent rate expressions, and ensures accurate representation of thermodynamic properties and multi-temperature energy exchange. Key features of PLPAK include ensuring a conservative energy balance through an enthalpy-based formulation for heat of reaction and consistently incorporating fast gas heating, super-elastic collision heating of electrons from vibrational relaxation, and other energy exchange modes. PLPAK with the developed plasma-kinetics reaction mechanism sets for $N_2 - O_2$ mixture is made publicly available to the scientific community and can be accessed at

A. Plasma Kinetics Model

1. Reaction Mechanism for $N_2 - O_2$

To describe the chemical kinetics associated with plasma decay, we extend the plasma kinetics model for pure N_2 based on references^{35,41,46}, incorporating accurate and self-consistent energy exchange in chemical reactions and between different modes to ensure energy conservation. The three-temperature plasma kinetics model for N_2 was validated against experimental measurements of electron density decay for a range of initial electron densities in our earlier work³⁶. The earlier work^{35,36} did not consider the distinction of electronically excited species of atomic nitrogen, which is used to explain the slow decay of electrons in nitrogen plasma by Popov⁴⁰ through associative ionization. Therefore, additional new species are included in the earlier model³⁵ to include associative ionization^{40,47,48}, and further addition of reactions and improvements are made to develop a complete reaction set for a $N_2 - O_2$ plasma system. Thus, we include a total of 24 species: N , N_2 , $N_2(A)$, $N_2(B)$, $N_2(C)$, $N_2(a')$, O , O_2 , $O(D)$, O_3 , NO , N^+ , N_2^+ , N_3^+ , N_4^+ , O_2^+ , O^+ , O_4^+ , NO^+ , O^- , O_2^- , $N(D)$, $N(P)$, and e^- .

The development of the reaction mechanism set is primarily based on the works of Kyossi³⁹, Shneider⁴⁹, and Popov^{40,50}. Additional reactions or necessary modifications from available literature data^{42,51-63} are incorporated into reaction rates to address inconsistencies in previous works, and elucidated as needed. The application of a second pulse can significantly elevate plasma temperatures, necessitating consideration of thermal dissociation, ionization, and atomic recombination, commonly required in weakly ionized plasma modeling in hypersonic flows. For such reactions, Park's⁵⁴ air-plasma reaction models are applied. Long-term electron decay is predominantly governed by ion-ion recombination due to Kyossi³⁹. Electron impact reactions are determined using BOLSIG+⁶⁴ to compute the electron energy distribution function, utilizing collision cross-section data available from the LaxCat database⁶².

Nitrogen atoms recombine to form electronically excited states of molecular nitrogen, as described by Popov⁵⁰ and Kyossi³⁹ in the reaction $N + N + M \rightarrow N_2(A, B) + M$. However, the reported rates for atomic recombination can be ambiguous when only a single value is provided without considering electronic excited states. Recent works^{42,51} independently present recombination rates for these processes, enabling differentiation between different electronic states. The electron impact dissociation rates from electronically excited states are sourced from Park⁵⁴. Notably, recombination rates for atomic nitrogen derived from both Park and modified Park models (refer to⁵⁶, Fig. 7) demonstrate tendencies to either significantly underestimate or overestimate at low temperatures (300 K). Conversely, the rates proposed by Campbell⁵⁹ for low-temperature plasma exhibit an overestimation at higher temperatures ($T > 2000$ K). Hence, a

combination of both sets of rates, adjusted for temperature, is utilized for atomic nitrogen recombination (R194). The formation of N_4^+ clusters is typically considered a three-body process. However, Troe⁵² demonstrated that it saturates into a two-body process, $N_2^+ + N_2 \rightarrow N_4^+$, at atmospheric pressure. Consequently, reaction R46 is formulated as a three-body process that saturates to a two-body process at 1 atm, with rates taken from⁵³. The N_2 -plasma kinetics model^{35,36}, upon which this work builds, lacked consideration for the distinction of electronically excited species of atomic nitrogen. Popov^{40,47,48} emphasizes the significance of these species in elucidating the slow decay of electrons in nitrogen plasma via associative ionization. To incorporate this pivotal process, which potentially holds relevance in dual-pulse laser energy deposition scenarios, where the second pulse augments the heating and coupling with the pre-ionized plasma channel, additional new species, namely N(D), N(P), and O(D), are integrated to account for associative ionization.

In the self-consistent plasma kinetics model, inconsistencies in rate expressions can lead to nonphysical changes in associated temperatures. This is because the heat of reactions relies on the difference between reactants and products' enthalpy, thus inconsistent rates contribute to additional errors in the energy equation. Such undesirable outcomes for specific reactions prompt the investigation and refinement of rate expressions, suggesting the inclusion of temperature dependence for such reactions. An example of this arises in the dissociative attachment of O_3 (R83). While rates from Kyossi³⁹ are provided as constants, reactions R83 (endothermic) and R84 (exothermic) involve considerable energy exchange, warranting improved rates and/or expressions. Rates with dependence on electron temperature (T_e) for R83-84 are provided by Cicman⁶³ and are used instead. Utilizing rates from Cicman⁶³, in reaction R83, for instance, a decrease in electron temperature results in a corresponding decrease in the rate, leading to stable electron temperature decay. Bodrov⁶⁰ suggested a three-body recombination mechanism for O_2^+ , indicating that it proceeds via dissociation to yield atomic oxygen. Hence, the rates for this process are obtained from Bodrov⁶⁰. Consequently, the reaction R72 is depicted as $2e^- + O_2^+ \rightarrow e^- + 2O$, rather than $2e^- + O_2^+ \rightarrow e^- + O_2$.

2. Thermodynamics and Transport

Thermodynamic properties are obtained from the NASA database⁶⁵, with enthalpy adjustments for electronically and vibrationally excited species using data from NIST spectroscopic resources⁶⁶ and partition functions from Therm4NEC⁶⁷. Mixture-averaged bulk gas transport properties, including mass diffusion coefficient, thermal conductivity, and viscosity, are determined using the mass-averaged mixing rule. Additionally, the mobility of species is required for multi-dimensional models. We utilize BOLSIG+⁶⁴ along with appropriate cross-sections⁶⁸ to determine electron mobility and collision frequencies. Experimental measurements take precedence for other ions when available; otherwise, the Langevin model is employed (Eq. 1). Here, α represents the

Table I. Reduced mobilities for ions in air plasma.

Ions	μ_0 [$\text{cm}^2\text{V}^{-1}\text{s}^{-1}$]	Ions	μ_0 [$\text{cm}^2\text{V}^{-1}\text{s}^{-1}$]
N^+	3.433	O_2^+	2.51
N_2^+	2.795	O_4^+	2.362
N_3^+	2.548	O_2^-	2.53
N_4^+	2.414	O^-	3.32
O^+	3.32	NO^+	2.65

polarizability of the mixture taken as $\alpha = 1.73\text{\AA}^3$ for air⁶⁹, and M is the reduced mass of the ion-neutral pair in atomic mass units. Data for other ions are shown in Table I^{69,70}.

$$\mu_0 = \frac{13.876}{(\alpha M)^{0.5}} \text{cm}^2\text{V}^{-1}\text{s}^{-1}; \quad \mu = \mu_0 \frac{760}{p_{\text{torr}}} \frac{T_K}{273.16} \quad (1)$$

3. Energy Exchange

$$Q_{ET} = \frac{3}{2} n_e k_B (T_e - T) (v_{en} + v_{ei}) \frac{2m_e}{m_h} \quad (2a)$$

$$Q_{EV} = \sum_{l=1}^{l_{\text{max}}} U_l K_l n_v n_e; \quad Q_{VE} = \sum_{l=1}^{l_{\text{max}}} U_l K_l^{\text{inv}} n_v n_e \quad (2b)$$

$$Q_{VT} = \frac{(E_v - E_v^0)}{\tau_{VT}}; \quad E_v(T_v) = \frac{n_v k_B \theta_v}{\exp\left(\frac{\theta_v}{T_v}\right) - 1} \quad (2c)$$

For elementary chemical reactions, heating values are derived from the enthalpy difference between reactants and products. Accurate thermodynamic property calculations, particularly species' enthalpy, are crucial within a multi-temperature framework, which are explained in section II A 2. Reactions with defined energy exchange ratios, which may lead to enthalpy disparities (e.g., intermediate species production), are balanced by redistributing energy across other modes when feasible³⁶. This approach ensures a conservative energy balance for all modes, while also seamlessly integrating fast-gas heating processes. Three-body reactions involving electrons as the third body contribute to electron heating. Vibrational excitation of ground-state molecular nitrogen through chemical reactions⁴⁰ is considered in reactions R14, R15, R36, R37, R185, and R186. Fast gas heating resulting from electron impact dissociation is explained by the formation of an intermediate excited species. Therefore, heating values for fast-gas heating in reactions R51, R191, and R192 are determined based on Popov's work⁵⁰. In addition to heat exchange in chemical reactive processes, other energy exchange terms Q_{ET} , Q_{EV} , Q_{VE} , and Q_{VT} are presented in Eq. 2, and they represent the heating rate due to elastic electron-molecule collisions, electron to vibrational excitation, vibrational relaxation to electrons, and vibrational relaxation to heavy particles, respectively.

$$v_{ei} = 3.636 \times 10^{-6} n_e T_e^{-3/2} \ln(\Lambda);$$

$$\ln(\Lambda) = 0.5 \ln \left(1 + \frac{\lambda_D^2}{r_{\text{ref}}^2} \right) \quad (3)$$

Here, v_{en} and v_{ei} represent the collision frequencies of electrons with neutrals and ions, respectively. v_{en} is calculated based on collision cross-sections using BOLSIG+, while the Coulomb collision frequency is approximated with Eq. 3⁷¹, where $\ln(\Lambda)$ is the Coulomb logarithm. For a vibrational level l , U_l denotes the excitation energy, K_l signifies the rate of vibrational excitation, and K_l^{inv} stands for the rate of vibrational to electronic relaxation, determined through the detailed balance principle using BOLSIG+. The first eight vibrational levels of N_2 are considered for the exchange processes Q_{EV} and Q_{VE} . Furthermore, n_v indicates the total number density of the corresponding species included for vibrational excitation, n_{vl} denotes the number density of vibrationally excited species at level l , τ_{VT} represents the effective vibrational-translational relaxation time based on the Landau-Teller formalism, and E_v denotes the total vibrational energy per unit volume, while θ_v refers to the characteristic vibrational temperature. The relaxation time undergoes significant changes for collisions with atoms. Thus, the effective relaxation time in Eqn. 2 is computed as $\tau_{VT} = (\sum_r X_r) \cdot (\sum_r X_r / \tau_r)^{-1}$, with the coefficients for determining individual relaxation times for various colliding partners obtained from Park⁷².

To prevent the Coulomb logarithm from becoming negative in laser-induced low-temperature plasmas, which occurs when $r_0 > \lambda_D$ in conventional formalism where $r_0 = e^2 / (4\pi\epsilon_0 m_e v_{th}^2)$ is the impact parameter and $\lambda_D = k_B T_e / (4\pi e^2 n_e)$ is the Debye length, we use the formulation proposed by Gericke et al.⁷³ based on hyperbolic trajectories (Eq. 3). This defines $r_{\text{ref}} = (\lambda^2 + r_0^2)^{1/2}$, where $\lambda = h / \sqrt{2\pi m_e k_B T_e}$ is the thermal de Broglie wavelength.

4. Model for Laser Coupling

Electrons in an electric field absorb energy with subsequent collisions through inverse-Bremsstrahlung absorption. A semiclassical treatment from Zeldovich and Raizer⁷⁴, Eq 4, is used here for the rate of absorption of energy per electron.

$$Q_{a,e} = \frac{e^2 I_L (v_{en} + v_{ei})}{m_e c \epsilon_0 (\omega_L^2 + (v_{en} + v_{ei})^2)} \quad (4)$$

$$v_i \approx \alpha^2 \beta \xi v_E; \quad \xi \approx 2\alpha \exp \left(-\frac{\alpha - 1}{\alpha} \left(\frac{6v^*}{v_E} \right)^{1/2} \right) \quad (5a)$$

$$v_{i,tot} = Q_{a,e} \beta \sum_k \frac{\eta_k X_k}{\tilde{I}_{p,k}} \quad (5b)$$

$$Q_a = n_e \left(Q_{a,e} - Q_{a,e} \beta \sum_k \frac{\eta_k X_k}{\tilde{I}_{p,k}} I_{p,k} \right) [Jm^{-3}s^{-1}] \quad (6)$$

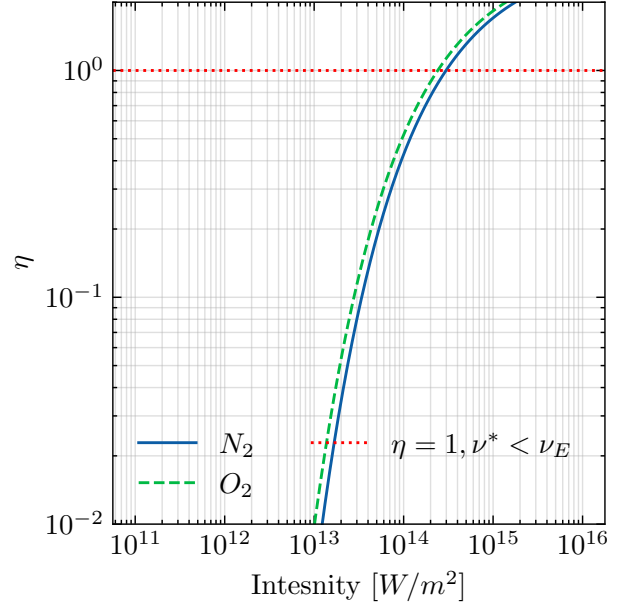


Figure 2. Avalanche ionization probability (η) as defined in Eq. 5.

Starting from the kinetic equation for the electron energy distribution function, Raizer⁷⁵ derives an approximate formulation for avalanche ionization frequency due to energy absorption through inverse Bremsstrahlung. For avalanche ionization, we consider multi-step ionization resulting from ionization of N_2 , O_2 , and NO . We define the energy-gaining frequency based on the time required for electrons to gain slightly more energy than ionization potential (≈ 1 eV above, denoted \tilde{I}_p), which gives $v_E = Q_{a,e} / \tilde{I}_p$. Raizer⁷⁵ provides two solutions for ionization frequency for cases, $v^* < v_E$ and $v^* > v_E$, where v^* represents the threshold energy for excitation. When the collisional loss of energy during energy absorption is significant (i.e., $v^* > v_E$), the avalanche ionization frequency changes, as the loss impedes ionization (see Eq. 5). X_k is the mole fraction of species k while $\alpha^2 = \tilde{I}_p / E^*$ (the fraction of ionization to the excitation thresholds). The parameter β is an empirical parameter representing the probability of ionization when the electron gains energy \tilde{I}_p from the electric field. Here, we take $\beta = 0.95$. At high intensities, we limit $\eta_k = 1$, thereby reproducing the limiting solution for $v^* < v_E$, i.e., $v_i \approx \beta v_E$. The parameters used for determining the avalanche ionization frequency include excitation threshold energies of 12.03 eV for N_2 and 9.40 eV for O_2 , along with ionization thresholds of 16.58 eV for N_2 and 13.06 eV for O_2 (note 1 eV more than the potential). Additionally, the averaged excitation rate for both species is considered to be 10^{-9} cm³/s based on results from BOLSIG+. η_{NO} was taken to be equal to η_{O_2} . The species production rate from avalanche ionization, calculated as $n_e \cdot v_i$, is incorporated as a source term in the corresponding species conservation equation. The net energy absorbed, Q_a , as defined in Eq. 6, is included as a source term in the electron energy equation.

Electron photodetachment induced by laser radiation contributes significantly to both electron generation and the loss

of negative ions. Specifically, we consider photodetachment from O_2^- and neglect those from O^- (threshold energy ≈ 1.4 eV)⁵ since the heating laser considered in this study operates at 1064 nm ($E_{ev} \approx 1.16$ eV). The cross-section for this process is described by $\sigma_{pd} = 10^{-4} \cdot E_{ev}(E_{ev} - 0.15)^{1.5} (0.370 \times 10^{-17} + 0.071 \times 10^{-17}(E_{ev} - 0.15)) [m^2]$ ⁷⁶. The corresponding source term in the species conservation equation has the form as shown in Eq. 7.

$$\left. \frac{dn_e}{dt} \right|_{pd} = - \left. \frac{dn_{O_2^-}}{dt} \right|_{pd} = \sigma_{pd} \frac{I_L}{E_J} N_{O_2^-} \quad (7)$$

The Keldysh parameter, or adiabaticity parameter, γ_k , is defined as the ratio of the laser frequency to the frequency of electron tunneling through the potential barrier, given by $\gamma_k = \omega \sqrt{2m_e I_p} / eE$, where ω represents the laser frequency, I_p is the ionization potential, and E denotes the electric field strength^{34,77}. Our study employs the Perelomov-Popov-Terent'ev (PPT) theory³⁴ to determine the photo-ionization rate (Ω_{hv}) in air under irradiation by a plane-polarized laser field. The intensity of the 1064 nm heating pulse is small for any noticeable photo-ionization. In the dual-pulse setup considered in this study, pre-ionization is generated using a fs laser with a wavelength of $\lambda = 800$ nm, a pulse width of $\Delta t_L = 100$ fs, and a beam waist radius of $\omega_0 = 150 \mu m$. The ionization yield is calculated based on the clamped laser intensity, determined by the balance between Kerr focusing ($\Delta n = \eta_2 I_{cl}$) and plasma defocusing⁷⁸. The calculated clamped intensity is $I_{cl} \approx 5.469 \times 10^{17}$ W/m² for air and $I_{cl} \approx 6.44 \times 10^{17}$ W/m² for nitrogen at atmospheric pressure.

B. Validation of the models

1. Plasma Kinetics

The plasma transport and hydrodynamics approach of the solver was validated in previous work³⁶. In this study, the extended plasma kinetics model is independently validated for air and pure nitrogen mixtures, as shown in Fig. 3. Note that in both cases, the same full reaction set is utilized. To validate the developed plasma kinetics model, initial conditions reflecting experimental data were employed. The intensity of the operating fs-pulse (100 fs, 800 nm) was varied to attain the desired total electron density at the end of the fs-pulse. This ensures a consistent relative population of ions, specifically N_2^+ and O_2^+ for air after fs preionization.

The method described by Papeer¹⁸ measures electron density by observing the reduction in microwave intensity as it propagates through the plasma, with the signal attenuation being proportional to the electron density. Chizov¹⁵ employed optical interferometry to estimate electron density by measuring changes in the plasma's refractive index. Comparison of the experimental results with the simulation results from this work shows good agreement in electron density decay profiles in pure nitrogen and air.

Table II. Threshold intensity for a single ns-pulse (1064 nm) breakdown ($n_e = 10^{21} m^{-3}$).

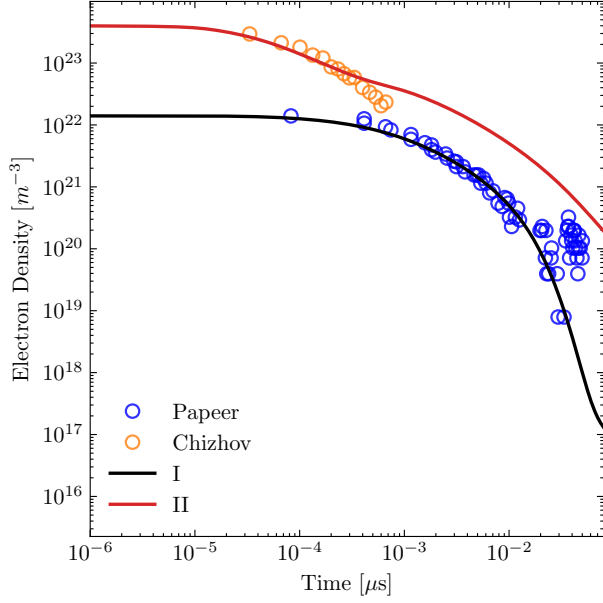
$n_{e0} [m^{-3}]$	$I_{n0} [GW/cm^2]$	Remarks
10^{12}	30.7	This work
10^{14}	26.60	This work
10^{14}	26.0	Yalin ¹⁰ (Modeling)
–	17.90	Yalin ¹⁰ (Experiment)

In addition to the comparison of the plasma decay in nitrogen (N_2) with Papeer's experimental measurements¹⁸, we also compared our results with the plasma kinetics model developed by Peters^{35,36} for pure nitrogen, which has been revised and extended in this study. The simulation results demonstrate that, while the overall decay of electrons remains largely unchanged, there is a noticeable slower plasma decay at longer times ($t > 10ns$) captured by the revised model. This is attributed to the incorporation of associative ionization processes, which involve electronically excited atomic nitrogen in the current work, as explained by Popov⁴⁰. It should be noted that such modification of the kinetics model allows us to capture electron decay dynamics more accurately, consistent with the experimental results of Papeer¹⁸ (see Fig. 3b).

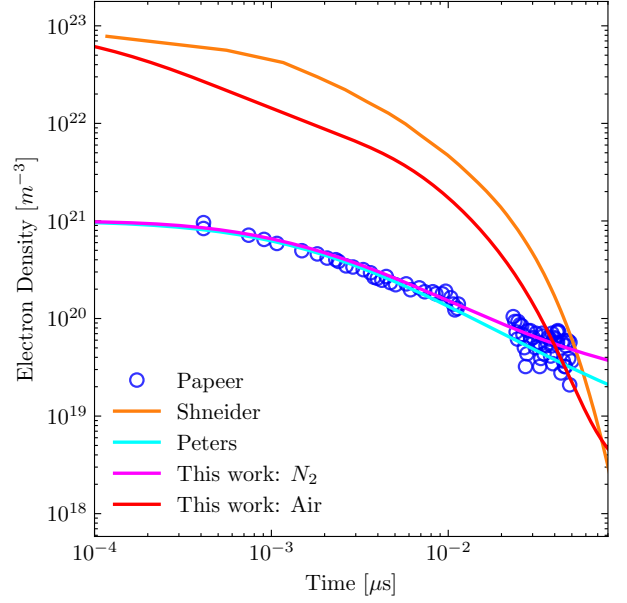
2. Laser coupling and breakdown

To validate the laser absorption part of the model, we refer to Yalin's experiments and modeling work on UV preionization for double-pulses¹⁰. The breakdown threshold criterion in the reference paper is based on the critical electron density of $10^{21} m^{-3}$. Although quantitative experimental measurements of the electron density were not reported, the work provided the experimental threshold intensity of breakdown (observed through strong light emission and sound) along with theoretical modeling results. Our comparison focuses on a single ns-pulse with a pulse width of 13 ns, utilizing a 1064 nm pulse. While Yalin¹⁰ employed a constant probability of avalanche ionization and a constant intensity model, we incorporate the temporal progression of the pulse intensity to ensure a smooth transition from low to high levels of avalanche ionization, by accounting for instantaneous changes in the probability of ionization based on the temporal intensity profile of the laser. We consider two initial electron densities of 10^{12} and $10^{14} m^{-3}$ and include the possibility of ionization from NO. The simulation results for the breakdown threshold intensity are shown in Table II and Fig. 4. Our findings align well with the results reported by Yalin, showing minimal variation with the initial electron density.

The previously defined breakdown criterion, based on a critical electron number density of $1 \times 10^{21} m^{-3}$, provides limited insight into the threshold intensity for controlled laser energy deposition. Further controlled energy addition over plasma of $10^{21} m^{-3}$ is still possible using a heating pulse. To establish a threshold beyond which additional energy deposition from the second pulse leads to a loss of control over the energy deposition process, we introduce a decoupling thresh-



(a) Comparison with experiments



(b) Comparison with various models models

Figure 3. Temporal evolution of electron density decay in fs-laser induced plasma filament at atmospheric pressure. Comparisons with Papeer¹⁸, Chizov¹⁵, and Peters^{35,36}.

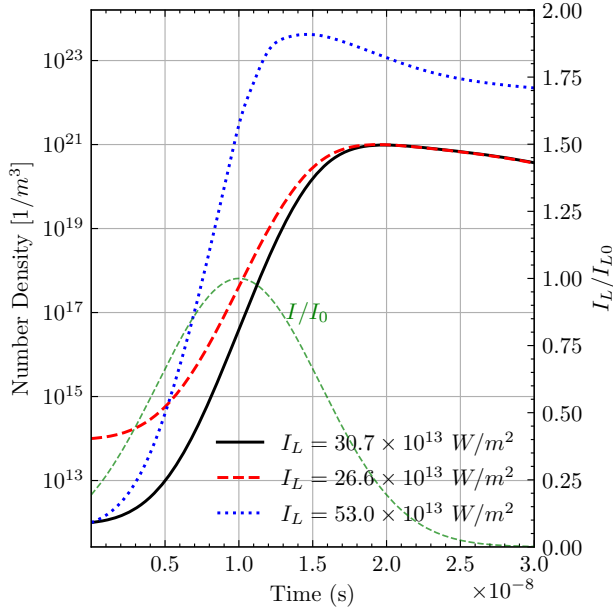


Figure 4. Temporal evolution of the electron density at various intensities of the ns-pulse, illustrating breakdown and decoupling thresholds in air.

old. The objective is to achieve controlled energy deposition, ensuring consistent and controlled plasma properties such as electron density, vibrational temperature, and gas temperature, without excessively heating the mixture ($T_g < 10000$ K). Thus, the aim is to determine the threshold at which the transition to uncontrolled absorption and breakdown occurs.

The decoupling threshold electron density is defined as the peak electron density at the plasma channel core, where the resultant refractive index gradient causes the laser beam to defocus, producing a deviation angle exceeding three degrees within a short distance ($\Delta x \ll L_p$). This short distance is taken as approximately 20 times the filament radius. The Eikonal approximation of the wave equation^{79,80} is employed to determine the required refractive index at the core, assuming a linear gradient. For a plasma filament radius of $50 \mu\text{m}$ and a wavelength $\lambda = 1064 \text{ nm}$, the threshold electron density is approximately $4 \times 10^{23} \text{ m}^{-3}$, corresponding to the required intensity of $53 \times 10^{13} \text{ W/m}^2$ at the core, as shown in Fig. 4. At these conditions the peak bulk gas temperature reaches $\approx 6000 \text{ K}$.

III. RESULTS AND DISCUSSION

In this section, we provide a detailed analysis of the temporal evolution of laser-induced plasma, focusing on the decay of fs-laser-generated plasma in air at atmospheric pressure to identify the dominant pathways and key reactions. We further assess the impact of oxygen addition in $\text{N}_2\text{-O}_2$ plasmas and examine the spatio-temporal evolution of laser plasma across various initial electron densities and temperatures. Additionally, we investigate the concept of dual-pulse techniques, specifically the coupling of laser energy from a ns heating pulse to the fs-laser induced filament. Particular attention is given to the temporal shaping of the ns heating pulse and its influence on plasma dynamics, as well as the efficiency of dual-pulse laser energy deposition.

A. Problem setup and initialization

Accurate determination of properties of the fs-laser filament requires modeling of the fs laser pulse propagation, which incorporates a nonlinear Kerr focusing effect, multiphoton and tunneling ionization, electronic excitation, wave dispersion, multi-filamentation and other optical phenomena. Although a detailed analysis of the fs laser pulse propagation is beyond the scope of this work, previous studies^{13,21,28}, have established some properties of fs-laser-induced filaments, particularly electron density, while reliable measurements of electron temperature and other species at the end of the pulse remain limited. The electron density in such filaments is primarily affected by the focusing setup and exhibits a saturation effect on the electron yield with the increase of the fs-laser energy⁸¹. Based on the saturation effect, we use the measured filament diameter ($\approx 100 \mu\text{m}$) observed in experiments to determine the decoupling threshold electron density. In the moderate focusing regime considered, the local intensity within the filament corresponds to the base clamping intensity (for self-propagating) augmented by an additional intensity, such that the final yield of electrons density at high energy saturates near the decoupling threshold. The clamped intensity and the corresponding electron density yield, based on the PPT theory, are detailed in³⁶. Figure 5 shows the electron density at the end of the fs-pulse for both air and nitrogen at 1 atm. Following ionization, free electrons absorb additional photons, and a simplified energy balance analysis is used to calculate the electron temperature as $T_e = (2/3)(h\nu_l(N_{ph} + N_{ph,+}) - I_p)$. Here, N_{ph} denotes the photons required for ionization, and $N_{ph,+}$ represents the additional absorbed photons. Assuming excess absorption of 2 and 4 photons in air-plasma, the resulting electron temperatures are 2.14 eV and 4.20 eV, respectively. The vibrational temperature is modeled solely for molecular nitrogen, and excludes other species.

B. Air Plasma Decay

The plasma decay dynamics in air are analyzed starting from the parameters of the fs laser filament at the end of the fs pulse. At the clamping laser intensity of $\approx 6 \times 10^{17} \text{ W/m}^2$, an electron yield of $\approx 10^{23} \text{ m}^{-3}$ is obtained, and an electron temperature (T_e) is set at 3 eV. After the end of the fs laser pulse, processes such as recombination, gas heating, and energy exchanges between various energy modes occur. Once sufficient thermalization is achieved, hydrodynamic expansion of the formed plasma channel occurs, which eventually cools over time due to diffusion processes.

To characterize the overall kinetic behavior of the plasma, the temporal scales of various collisional processes are evaluated. The characteristic timescale (τ) is determined using the chemical kinetic rate expression $\tau = (\omega_k/n_e)^{-1}$, where ω_k denotes the reaction rate of the k th chemical process. The results of this analysis are presented in Fig. 6 for the main reactions in air plasma and in Fig. 7 for electron energy loss reactions, with detailed descriptions of the specific reactions provided in Table III. The key kinetic processes governing FLI plasma

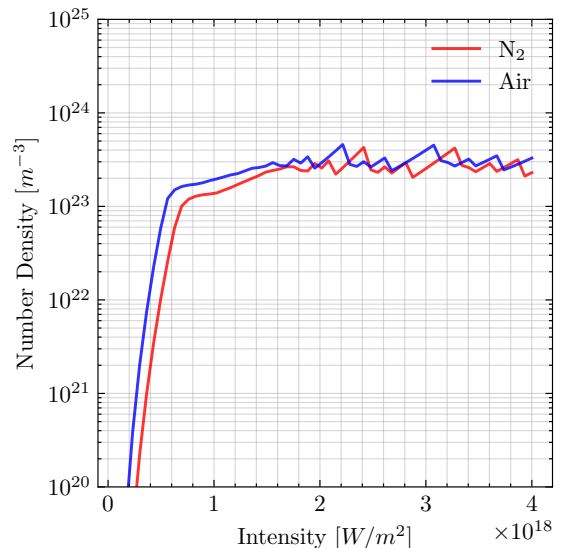


Figure 5. Number density of electrons generated in the fs-laser filament in nitrogen and air. Tighter focusing results in saturation at higher electron density.

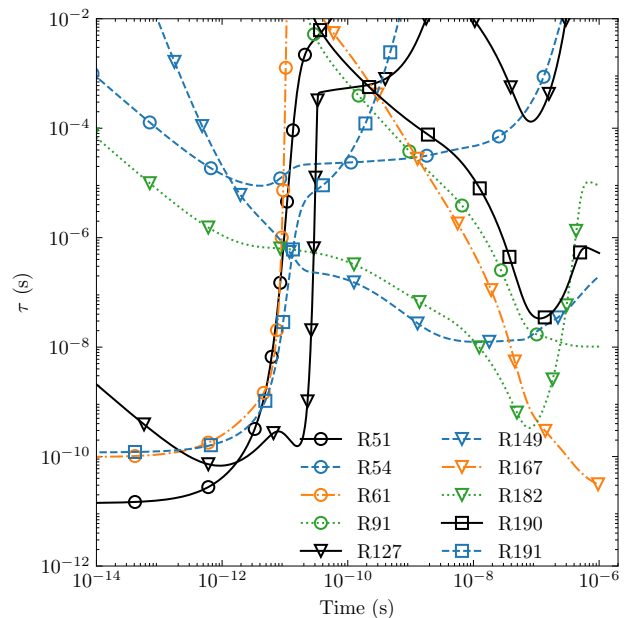


Figure 6. Temporal scales of main reactions in the fs-laser induced plasma in air at atmospheric pressure.

decay in air are identified as follows:

- Elastic collisions between electrons and heavy particles (Q_{ET}) occur rapidly with $\tau \approx 10^{-12} \text{ s}$, as do vibrational excitations (Q_{EV}) with $\tau \approx 10^{-11} \text{ s}$.
- Initially, electron impact dissociation of neutrals is significant (e.g. R51, R191), with a high rate at early times, $\tau \approx 10^{-11} - 10^{-10} \text{ s}$, leading to a buildup of atomic nitrogen and oxygen.

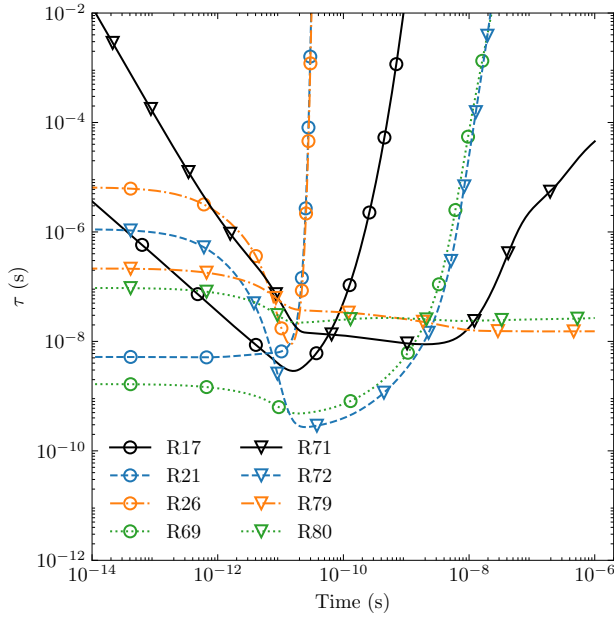


Figure 7. Temporal scales of main reactions involving the loss of electrons in the fs-laser-induced plasma in air at atmospheric pressure.

- Cluster ion formation of N_4^+ peaks around 10 ps, coinciding with the peak formation of NO^+ (R127).
- Dissociative recombination of N_2^+ and O_2^+ along with electronic excitation of molecular nitrogen occur within $\tau \approx 10^{-10} - 10^{-9}$ s. Note that for pure nitrogen the recombination with N_4^+ is the main channel for decay at ns timescales thereby producing high population of $N_2(B)$ but this is weak in air-plasma because of less population of N_4^+ .
- Attachment operates on a timescale of about $\tau = 10^{-8}$ s, remaining relatively constant throughout the decay process. Electron recombination with NO^+ also has a $\tau = 10^{-8}$ s timescale, but only lasts for tens of nanoseconds.
- NO formation begins slowly through ion-ion neutralization of NO^+ and O_2^- (R149) until 10 ns. After 10 ns, with sufficient accumulation of electronically excited $N(D)$, rapid NO production occurs via $N(D)$ recombination (R182). NO is primarily consumed through dissociation (R167) after 100 ns.
- Detachment becomes prominent after significant attachment and operates on a $\tau = 10^{-8}$ s timescale but emerges around 100 ns. At around 100 ns, the relaxation of electronically excited atoms and associative ionization occur, resulting in a decrease in density of the excited atoms.
- Various atomic recombination processes become significant after several hundreds of nanoseconds.

Thus, plasma decay dynamics can be divided into early ($t < 10^{-11}$ s), mid ($10^{-11} \text{ s} < t < 10^{-9}$ s), and late ($t > 10^{-9}$ s) stages, based on the timescales of various processes, as illustrated in Fig. 7. In the early stage, two-body dissociative recombination predominates (R69, R21, R22), while dissociative recombination from clusters and three-body recombination with O_2 (R72, R75) dominate the mid-stage. Two-body dissociative recombination of O_2^+ (R69) significantly affects both early and mid-stages. The late-stages begin with a prominent recombination with NO^+ (R71), followed by attachment reactions (R79, R80), which drive the remainder of the late stage. In air plasma, electron production beyond 10 ns is primarily controlled by detachment in collisions with oxygen (R91) and associative ionization (R190), with characteristic timescales of approximately 10 ns, which slows down the plasma decay. The main reactions depicted in the figures 6 and 7 are summarized in table III, and the complete set of reactions is presented in the appendix.

Table III. Main reactions in air-plasma as presented in Figures 6 and 7.

ID	Reaction	ID	Reaction
R17	$N_4^+ + e^- \rightarrow N_2 + N_2(B)$	R21	$N_2^+ + e^- \rightarrow N + N(D)$
R26	$N_2^+ + 2e^- \rightarrow N_2 + e^-$	R51	$N_2 + e^- \rightarrow N + N(D) + e^-$
R54 ^a	$N_2(A, v) + e^- \rightarrow N_2 + e^-$	R61	$N_2 + e^- \rightarrow N_2(C) + e^-$
R69	$O_2^+ + e^- \rightarrow 2O$	R71	$NO^+ + e^- \rightarrow N + O$
R72	$O_2^+ + 2e^- \rightarrow 2O + e^-$	R79	$2O_2 + e^- \rightarrow O_2 + O_2^-$
R80	$N_2 + O_2 + e^- \rightarrow N_2 + O_2^-$	R91	$O + O_2^- \rightarrow O_3 + e^-$
R127	$N_2^+ + O \rightarrow N + NO^+$	R149	$N_2 + NO^+ + O_2^- \rightarrow N_2 + NO + O_2$
R167	$N + NO \rightarrow N_2 + O$	R182	$N(D) + O_2 \rightarrow NO + O(D)$
R190	$N(P) + O \rightarrow NO^+ + e^-$	R191	$O_2 + e^- \rightarrow 2O + e^-$

^a $v \in [0, 4]$. See the complete reaction mechanism for details.

The temporal decay of various species (neutrals, electrons, ions, and electronically excited species) in the fs-laser induced filament in air at atmospheric pressure, taken at the core of the plasma channel, is illustrated in figures 8 and 9. The subsequent temporal evolution of gas, vibrational, and electron temperatures is depicted in Fig. 10. Observations indicate a higher concentration of atomic oxygen compared to atomic nitrogen during the early stages of plasma decay, primarily due to dissociative recombination and electron impact dissociation. Both processes result in the rapid production of atoms within nanoseconds for oxygen and even faster for nitrogen.

The maximum density of NO is reached at approximately 50 ns. Electronically excited states of nitrogen, particularly $N_2(A)$ and $N_2(B)$, show a rapid decrease within the first few nanoseconds, reaching low concentrations of about $1.0 \times 10^{16} \text{ m}^{-3}$ around 100 ns. For pure nitrogen, the decay timescale of the ground electronic state of atomic nitrogen reported in literature⁸² is approximately 100 μs . In air plasma, the decay occurs on the μs timescale due to faster quenching in the presence of oxygen. All electronically excited atomic states exhibit a sharp decay around 100 ns. A slight drop in the bulk density during shock detachment caused by the hydrodynamic expansion of the plasma channel is observed around

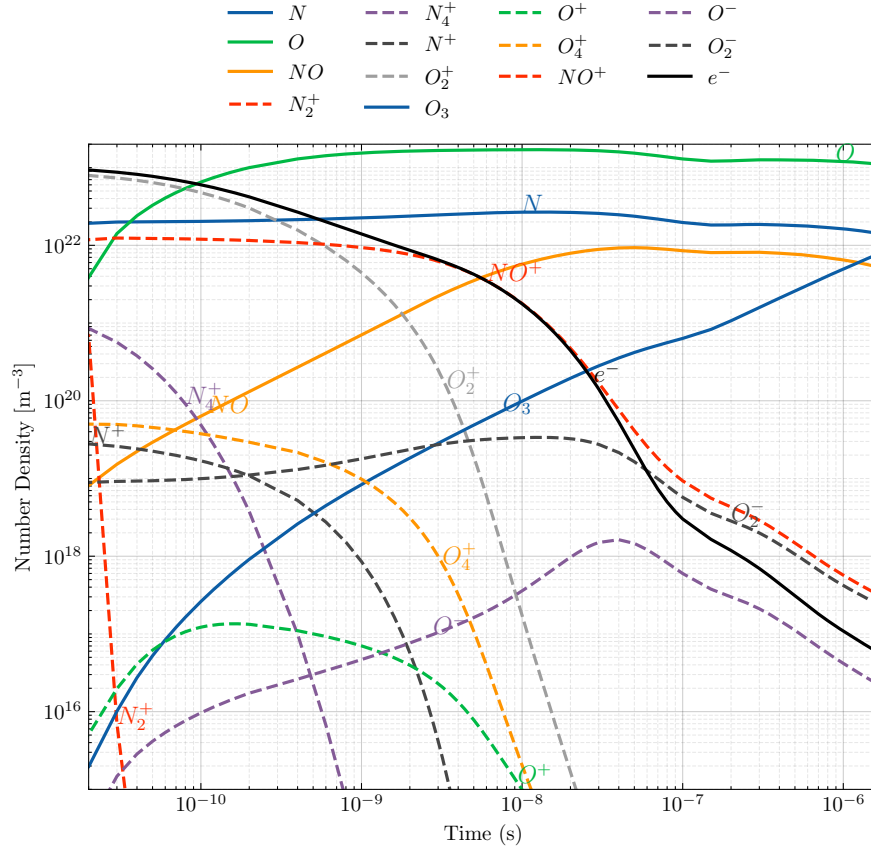


Figure 8. Temporal evolution of number densities of various species, including ions, at the center of the fs-laser induced plasma in air at atmospheric pressure.

100 ns on the decay profiles of atomic and molecular nitrogen and oxygen.

1. Analysis of energy exchange channels

With an initial electron temperature of 3 eV in the fs-laser filament, electron impact processes, including dissociation (R51) and electronic excitation (R61, R191), dominate the initial electron energy loss within the first 10 ps, while vibrational excitation (Q_{EV}) plays a minor role. After 10 ps, Q_{EV} becomes the primary electron energy loss mechanism and partially restored by three-body dissociative recombination (R72), superelastic pooling from electronically excited N_2 (R62), and energy transfer from vibrationally excited N_2 (Q_{VE}).

The electron temperature equilibrates with the vibrational temperature over time. Gas heating from electron impact dissociation and dissociative recombination peaks at 50 ns, followed by cooling due to the hydrodynamic expansion of the plasma channel. The development and radial propagation of the shock wave are seen in density profiles at various times. For the same initial electron density, the vibrational temperature of N_2 is higher in air than in nitrogen, as the presence of atomic oxygen enhances the recombination of atomic nitro-

gen into vibrationally excited N_2 . The lower ionization potential of air further reduces energy absorption from the fs-laser pulse, leading to a lower peak gas temperature compared to nitrogen.

C. Spatial profiles and refractive index dynamics

For multiple pulse applications and wave-guiding, the spatial distribution of species such as electrons, O_2^- , and NO is critical for controlled coupling via spatially shaped pulses. Dynamics of the refractive index in the formed plasma filament is also critical for waveguiding and optical diagnostic applications. Thus, in this part, we concentrate on the radial distribution of species and corresponding changes in the temporal dynamics of the refractive index. As shown in the temperature, Fig. 10, and bulk gas density profiles, Fig. 11, thermalization induces a weak shock wave propagating radially outward. The radial distribution of electrons and O_2^- in Fig. 12 and NO in Fig. 13 shows different profiles. Electrons maintain a Gaussian-like central profile, expanding at the edges, while NO follows a near-Gaussian distribution. In contrast, O_2^- accumulates at the plasma edge. After 100 ns, the peak for O_2^- shifts from the center towards the radial edge. This local peak in O_2^- concentration at the radial interface re-

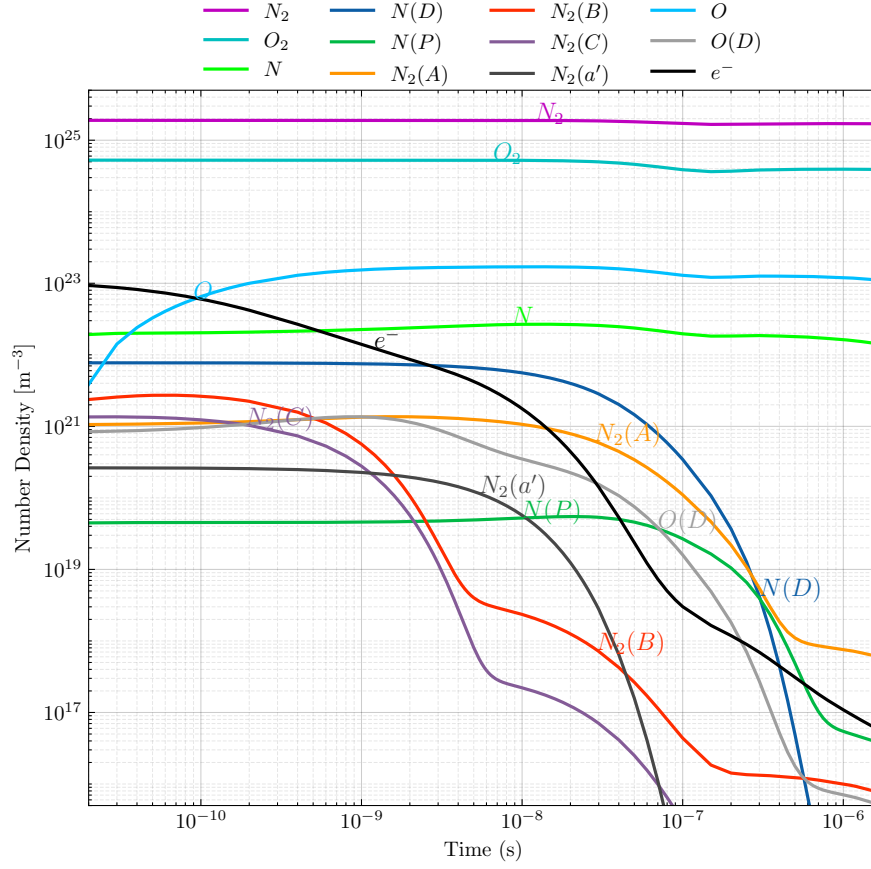


Figure 9. Temporal evolution of number densities of various species, including electronically excited states, at the center of the fs-laser induced plasma in air at atmospheric pressure.

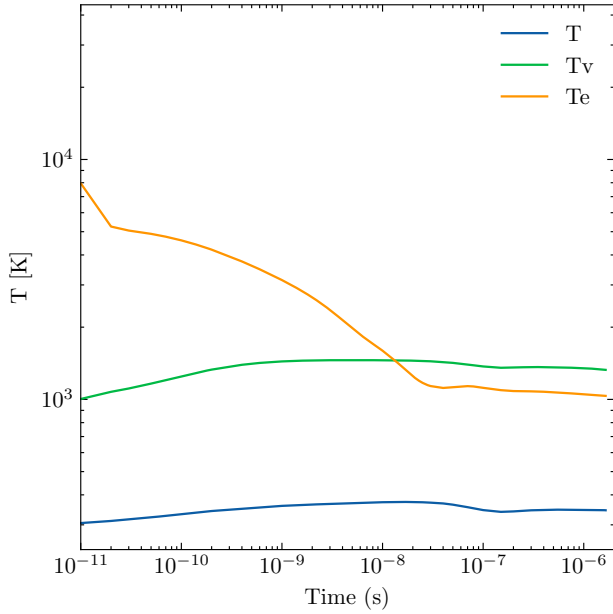


Figure 10. Temporal evolution of the bulk gas temperature T , vibrational temperature T_v , and electron temperature T_e at the core of the fs-laser induced plasma channel in air.

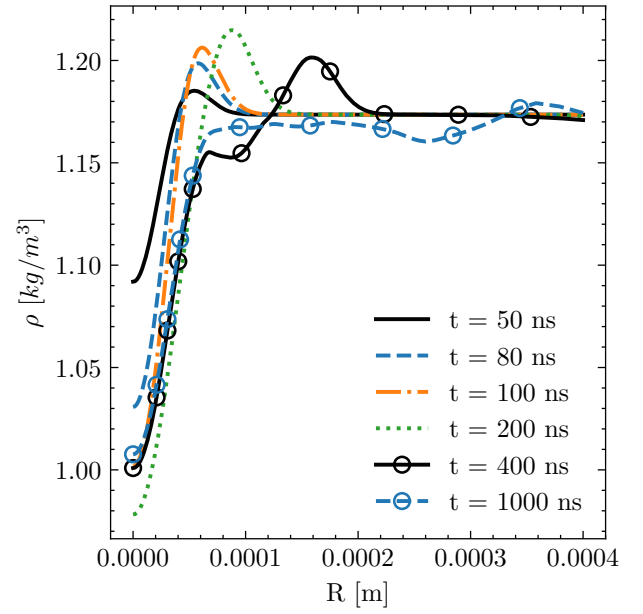


Figure 11. Radial distribution of the bulk gas density at various times during the decay of the fs-laser induced filament in air.

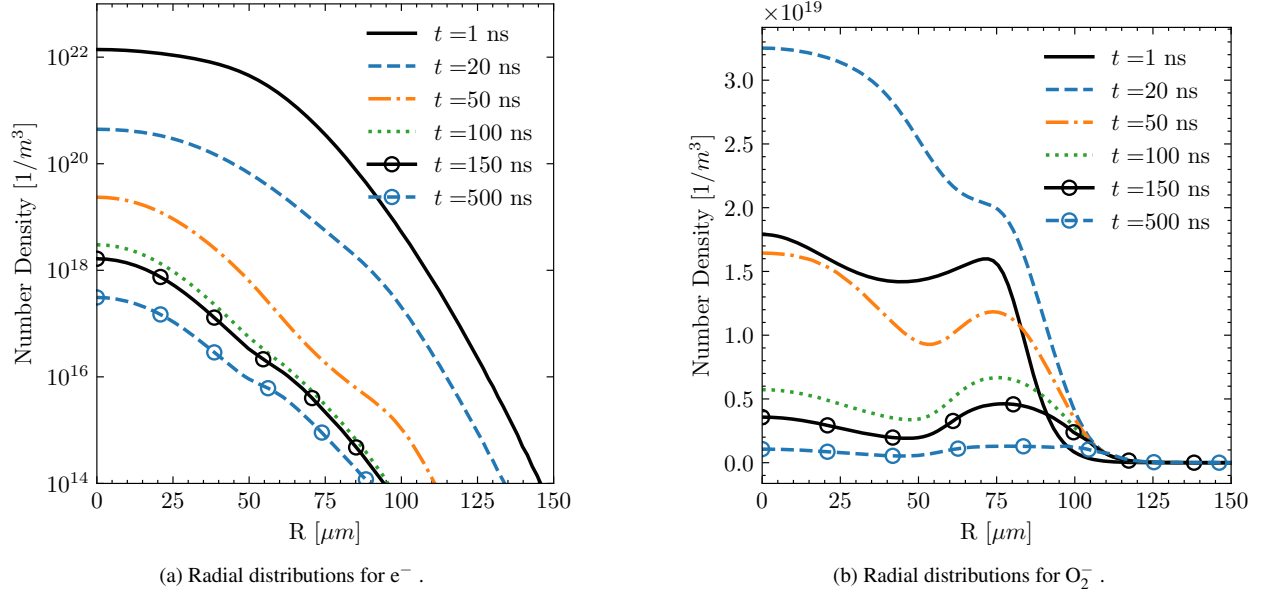


Figure 12. Radial distribution of number density of electrons and O_2^- at various times for the fs-laser induced filament in air.

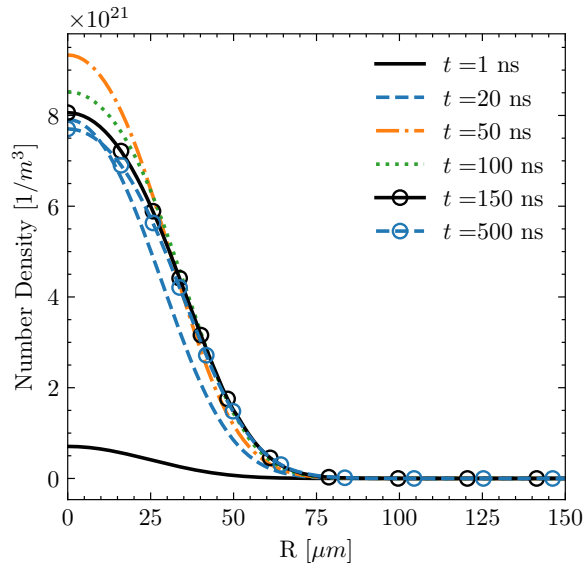


Figure 13. Radial distribution of the number density of NO at various times for the fs-laser induced filament in air.

sults from the negative ion compression by ambipolar electric fields, as explained in³⁶.

All these processes result in dynamical changes in the refractive index during the plasma decay in the fs-laser filament. Figure 14 shows the contribution of various species and processes in air refractivity. Initially, the refractive index is dominated by electron contributions, but a gradual shift to the hydrodynamic-dominant contribution is observed. A dip in the refractive index after the fs pulse is caused by the high electron density, after a rapid electron decay the refractive index returns to near-ambient levels at 10 ns. A reappearance of

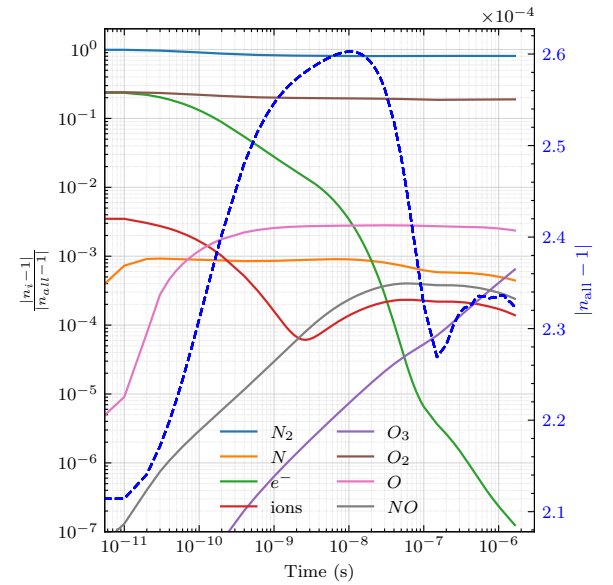


Figure 14. Refractive index contributions during the fs-laser plasma decay in air at atmospheric pressure for the wavelength of 1064 nm.

the dip occurs around 100 ns due to the plasma channel expansion. The contribution from dissociated oxygen exceeds that of nitrogen, highlighting the importance of considering dissociation in electron density measurements, particularly using interferometry⁸³. The gradual increase in O_2^- contribution is attributed to its density growth and its threefold higher polarizability compared to molecular oxygen. Additionally, the contributions from ions and NO exceed those from electrons after about 30 ns.

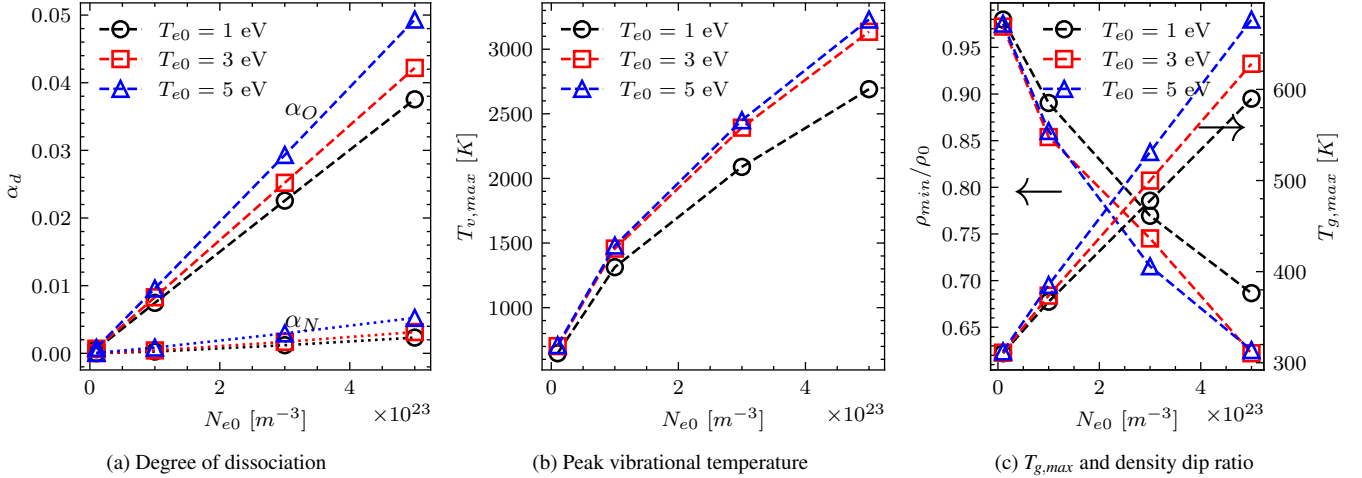


Figure 15. Characteristic properties of the fs laser filament in atmospheric pressure air for various initial electron densities and electron temperatures.

D. Plasma characteristics at various initial conditions

The characteristics of the fs laser filament, including its initial electron density and temperature, are primarily dictated by the laser focusing setup²¹. In this analysis, electron density is considered within the range of 10^{22} to $5 \times 10^{23} \text{ m}^{-3}$ and electron temperature between 1 and 5 eV, with a focus on plasma decay properties and the influence of molecular oxygen (O_2). Plasma decay properties, including dissociation fraction, vibrational excitation, bulk density dip, and gas temperature, are examined and illustrated in Fig. 15. The analysis reveals that the dissociation fraction of oxygen exceeds that of nitrogen significantly. The increase of the electron density and temperature both enhance the rate of electron impact dissociation (see R51, R191). Moreover, the reaction's progression rate exhibits a linear dependence on the electron density. Elevated electron temperatures decrease rapidly due to energy loss from various channels, as previously discussed in section III B 1. For $T_e > 1$ eV, vibrational excitation rates plateau, and vibrational temperature saturates, similar to observations in nitrogen⁸³, becoming independent of the initial electron temperature while varying with the initial electron density. A linear dependence of the bulk gas temperature on the initial electron density is observed with a stronger density dip due to higher thermalization, which is similar to the behavior observed during the decay of nitrogen plasma⁸³. For identical plasma conditions, i.e., n_e and T_e , the gas temperature in nitrogen plasma is higher than in air due to the greater energy required for nitrogen ionization. Gas temperature measurements in air-plasma filaments based on the N_2 second positive system reported temperatures in the range of 400–550 K^{8,19}. In a filament with a tighter focusing setup, Blanchard *et al.*²⁷ measured a vibrational temperature of approximately 2700 K, which corresponds to an electron density of $4.0 \times 10^{23} \text{ m}^{-3}$ and T_e of 3 eV in Fig. 15. Our recent Thomson scattering measurements⁴⁴ showed that for an initial electron density of $\approx 5.0 \times 10^{23} \text{ m}^{-3}$, the gas temperature was about 700–800 K.

A similar temperature of 700 K for $T_e = 5$ eV is observed in our results for $n_e = 5.0 \times 10^{23} \text{ m}^{-3}$.

There is a possibility of vibrational excitation of molecular oxygen, with a much shorter VT relaxation time, about 100 ns, compared to nitrogen, which could explain the anomalous rise in the gas temperature around 100 ns²⁹. But an additional equation for the vibrational excitation of O_2 has not been included in the model because of the absence any experimental measurements of the vibrational population of O_2 . However, the conclusions presented remain valid, as the temperature increase is significant only for cases with the high initial electron density. Even in these cases, while the temperature increase may be present due to the vibrational relaxation of O_2 , it does not exceed the peak thermalization temperature.

Now we assess the influence of oxygen on the plasma decay in the fs laser filament. Here, a laser pulse intensity of approximately $7 \times 10^{17} \text{ W/m}^2$ is maintained, resulting in an electron density of 10^{23} m^{-3} at the end of the fs pulse for nitrogen (N_2), with oxygen concentrations adjusted to 0.1%, 2%, and 22%. A comparison is also made with the plasma decay in air, ensuring a final electron density of 10^{23} m^{-3} . Under these conditions, varying O_2 concentration only slightly affects the electron density yield from the fs-laser. The temporal decay of electrons is shown in Fig. 16. Nitrogen exhibits faster decay compared to air within the first few ns, given the same initial electron density. After 10 ns, electron attachment processes dominate in air, leading to a sharper plasma decay compared to that in nitrogen.

A sustained higher plasma density is observed for an extended time when a small percentage of O_2 (around 2%) is added. The main reason for this extension of the plasma life is that a significant portion of added O_2 becomes ionized, resulting in a strong production of atomic oxygen from dissociative recombination. Since the molecular oxygen concentration is too small, attachment is not significant, because the main channel for attachment is a three-body process, $2 \text{O}_2 + e^- \rightarrow \text{O}_2 + \text{O}_2^-$ with quadratic dependence on O_2 . As

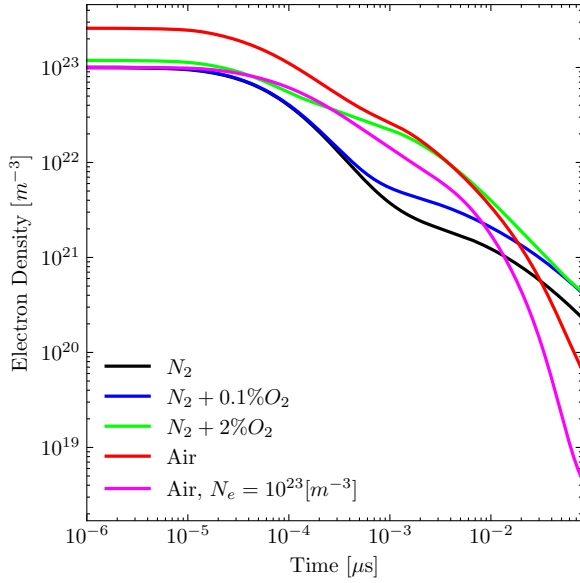


Figure 16. Electron density dependence on time in the fs-laser induced plasma in a mixture of $N_2 - O_2$ for various concentrations of O_2 at atmospheric pressure.

a result, attachment does not significantly affect the plasma decay in current conditions. At the same time, the presence of atomic oxygen enables associative ionization, such as $N_2^+ + O_2 \rightarrow NO + e^-$, which slows down the plasma decay. As electron attachment processes intensify with the increase of O_2 , they eventually overcome the effect of associative ionization, resulting in the faster decay rates in air. Earlier experimental work⁸⁴ using microwave scattering to capture the dynamics of electron density has shown a similar trend of slowed decay with the addition of a small percentage of O_2 , highlighting the importance of associative ionization in air-plasma kinetics.

E. Laser energy coupling to the fs laser filament

Filaments induced by fs-lasers are repeatable and characterized by slender structures that can extend beyond the Rayleigh length. Controlled coupling of an ns heating pulse with these filaments offers potential for novel applications. The relevant findings are presented here. This section explores the plasma characteristics from both single laser pulse and dual laser pulse setups and identifies the main kinetic processes that characterize dual-pulse laser plasmas. The revival of the laser plasma using the dual-pulse approach, its dependence on the time delay between the two pulses, and the temporal shaping of the ns pulse intensity for optimal pairing of fs and ns pulses are also explored.

1. Plasma generation with single pulse and dual Pulse

Laser-induced plasma generates thermal, chemical, and hydrodynamic effects, important for various applications. The extent of thermalization depends on the ionization degree, with electron densities exceeding $10^{21} m^{-3}$ producing significant effects. Here we focus on achieving an electron density of $10^{23} m^{-3}$ and investigating the selectivity of the plasma properties and avoiding breakdown. The plasma is generated using both a single ns 1064 nm pulse (SP) and a dual fs-ns pulse (DP; 800 nm, 1064 nm). For simplification, the ns pulse is assumed to have a constant intensity and a 15 ns pulse duration. The fs pulse generates the plasma with $n_e = 10^{23} m^{-3}$, $T_g = T_v = 300$ K, and $T_e = 3$ eV. This fs-plasma channel decays rapidly and requires revival to $n_e = 10^{23} m^{-3}$ with the second heating pulse. In single ns-pulse operation, the electron density is achieved assuming an initial electron density of $10^{12} m^{-3}$ (see Fig. 4 for cases with different initial electron densities).

The electron density time history for SP and DP is shown in figures 17a and 17b, respectively. The simulation results, shown in Fig. 17, indicate that the laser intensity required to achieve an electron density of $10^{23} m^{-3}$ is 30 GW/cm² for a single ns-pulse (SP) and 17.2 GW/cm² for dual fs-ns pulses (DP). Additionally, the results in Fig. 17 include a 10% intensity variation for both configurations shown by the dashed and dotted lines. The DP configuration offers improved controllability over the SP setup, with smaller variations in electron density caused by fluctuations in operating conditions (modelled as a 10% intensity variation). Temporal dynamics of the bulk gas and vibrational temperature (not shown) also lead to the same conclusion, with DP being less sensitive to variations in operating conditions. This results in better repeatability of plasma generation and more effective prevention of uncontrolled breakdown. The DP configuration also improves electron decay dynamics, leading to a slower decay rate after the second heating pulse, as seen in Fig. 17b.

2. Main processes of dual-pulse laser energy coupling

Fig. 17b shows a reduction in the plasma decay rate after revival for the DP configuration compared to the SP configuration, despite the same peak electron density. The key question is what kinetic processes are responsible for the slower plasma decay and the laser energy coupling by the ns laser pulse to the fs laser plasma. To answer this question, we evaluate the degree of the enhancement of the kinetic rates caused by the ns heating pulse utilizing the analysis of normalized rates of the electron production. These rates are defined by Eqn. 8. It's worth noting that in this context, the SP refers to the plasma generation with a fs-laser pulse.

$$[\text{Normalized Rate}]_k = \left\| \frac{\left(\frac{dn_e}{dt} \Big|_{DP} - \frac{dn_e}{dt} \Big|_{SP} \right)_k}{\frac{dn_e}{dt} \Big|_{SP}} \right\| \quad (8)$$

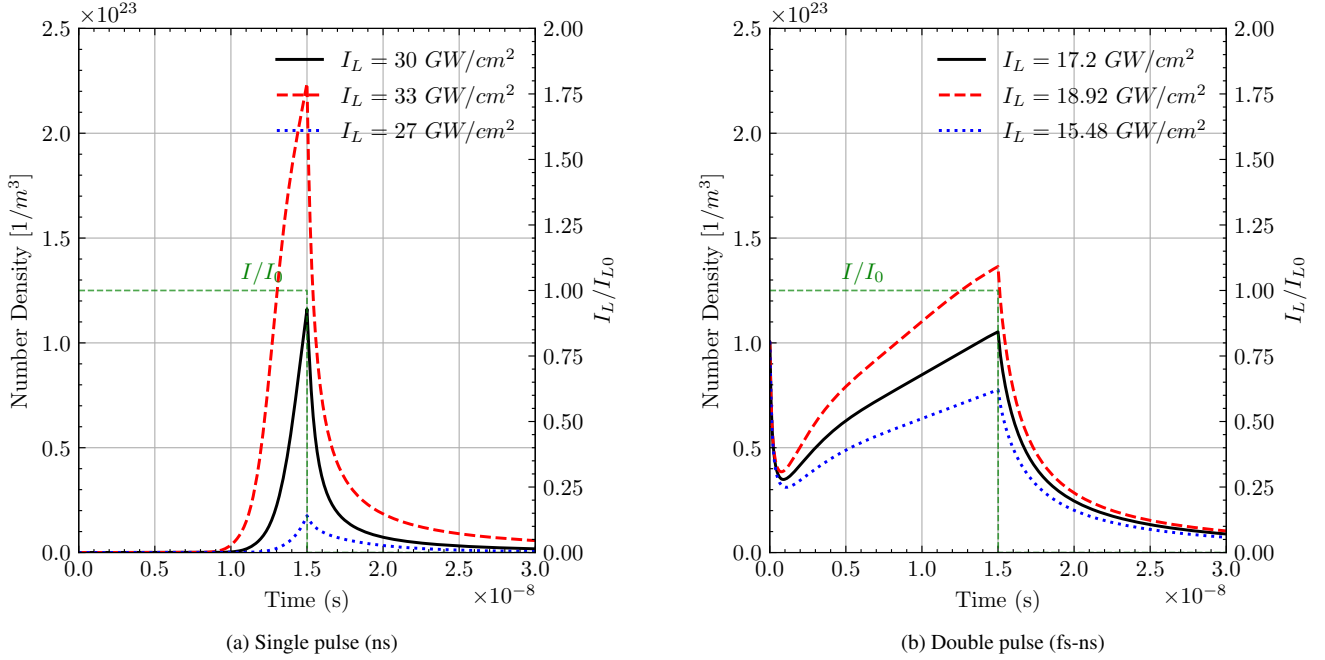


Figure 17. Laser-induced plasma formation from single ns-pulse and double fs-ns pulse configurations.

For a single fs-filament the main kinetic channels counteracting electron decay are associative ionization (R190), detachment with O_2 collisions (R91), and detachment with O_2^- collisions (R86). The primary kinetic process for electron consumption is dissociative recombination (R69), which dominates initially. However, associative ionization and detachment become significant after 10 ns. The heating pulse introduces additional processes for electron production, which include avalanche ionization and photo-detachment. The normalized rates for various electron source terms at the laser intensity of 17.6 GW/cm^2 are shown in Figure 18. During the second pulse (heating ns-laser pulse), avalanche ionization and photo-detachment dominate, with minimal contributions from other processes. At lower laser intensities (around 1 GW/cm^2 , not shown), photo-detachment contributes even more to the production of electrons than avalanche ionization. After the pulse begins, associative ionization and detachment show significant increases in contribution. The reduction in the recombination rate, caused by the high electron temperature, has a negligible effect. Associative ionization and detachment are the dominant channels, slowing the plasma decay after the heating ns-laser pulse.

A critical aspect of energy coupling by the ns pulse to the fs laser filament is the vibrational excitation of nitrogen molecules due to electron-neutral collisions. After the ns-laser pulse, energy transfer from excited vibrational states to free electrons (Q_{VE}) also increases, which helps to sustain relatively high electron temperatures and provides an energy source to the bulk gas through vibrational-translational relaxation. Figure 19 shows the temporal evolution of vibrational temperature and the source term Q_{VE} at various laser intensities, for cases with and without the second laser pulse (ns-laser

). At lower laser intensities ($\approx 1 \text{ GW/cm}^2$), the enhancement of the source term Q_{VE} due to inelastic collisions is negligible compared to higher laser intensities. Although the direct influence of the electron temperature on the plasma decay dynamics is minimal^{13,36}, the time dependence of electron and vibrational temperatures is important for determining the amount of laser energy stored in vibrational degrees of freedom, an established channel for the subsequent relaxation of energy to the bulk gas.

3. Plasma revival by the ns laser pulse

Experimental observations show that increasing the ns pulse energy to revive high plasma density often leads to stochastic breakdown³⁰. However, sustaining laser plasmas at relatively high electron densities, such as $n_e = 10^{21} \text{ m}^{-3}$, is essential for applications requiring precise plasma parameters at low gas temperatures while reliably avoiding breakdown. The results presented here on revival of plasma were reported in the AIAA SciTech conference proceedings⁸⁵.

Figure 20a illustrates the time evolution of electron density following laser energy deposition by fs and ns laser pulses in atmospheric pressure air. Simulation results for various time delays between fs and ns pulses, ranging from 0 ns to 50 ns, indicate that maintaining a constant electron density requires a slight increase in ns pulse intensity in air. In nitrogen, the laser intensity needed to sustain $n_e = 1.0 \times 10^{21} \text{ m}^{-3}$ remains relatively independent of the time delay between pulses, but the required ns pulse energy is higher than in air due to faster recombination channels, particularly N_4^+ recombination, which dominates at early times. As electron density decreases, the

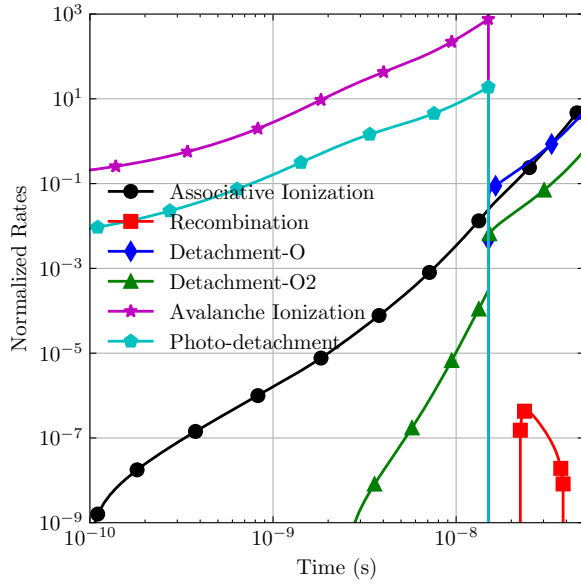


Figure 18. Normalized rates (Eq. 8) for various electron source terms for a dual-pulse laser plasma at the laser intensity of 17.6 GW/cm^2 .

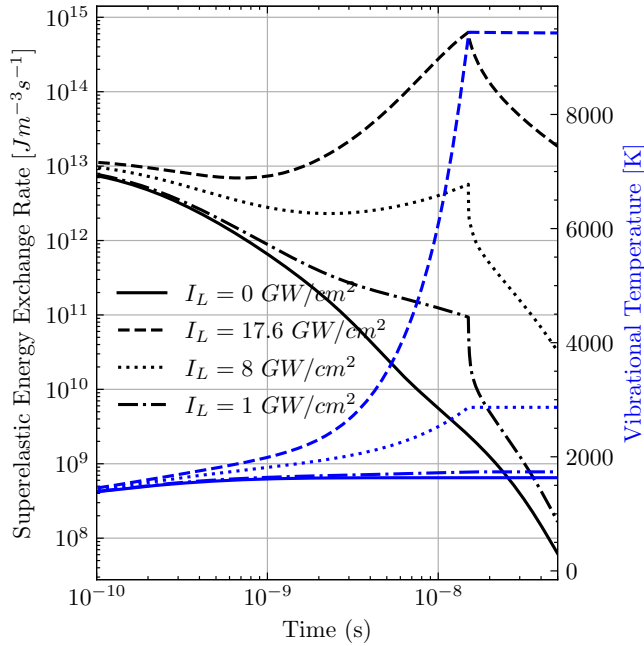


Figure 19. Superelastic energy exchange rate (Q_{EV} , left axis) and vibrational temperature (right axis) for a single fs-pulse ($I_L = 0$) and fs-ns laser pulses.

influence of the N_4^+ recombination channel diminishes. In air, the lower ionization potential of oxygen and the presence of O_2^- facilitate photo-detachment under the ns heating pulse, reducing laser energy requirements compared to plasma revival in nitrogen.

Laser intensity variations of $\pm 20\%$ are incorporated into the simulations to model realistic fluctuations observed in experiments. The base laser intensity required to sustain the

desired plasma density, shown in Fig. 20a, serves as a reference. Figure 21 presents the electron density at the end of the ns pulse, indicating that in nitrogen plasmas, electron density variations remain largely independent of the time delay between pulses. In air plasmas, longer time delays lead to greater deviations from the base electron density for the same intensity variations. At higher laser intensities, the electron density remains within $n_e \sim 3.0 \times 10^{21} \text{ m}^{-3}$, while at lower intensities, similar electron densities are maintained for time delays up to 20 ns, with a more pronounced drop at longer delays, though still within an order of magnitude of the base case. A 20% increase in laser intensity results in only a slight rise in electron density, reducing the risk of uncontrollable breakdown. Earlier experimental work⁸⁵ demonstrated a repeatable and reliable revival of plasma in nitrogen using ns-laser pulse heating without transition to breakdown. The results showed that peak electron density was reached with minimal dependency on the delay, consistent with the observations in this study. These results demonstrate the effectiveness of the dual-pulse laser approach in sustaining plasmas at the desired electron density below the breakdown threshold.

4. Temporal delay and shaping of ns laser pulse

Finally, we concentrate on the optimization of the dual-pulse laser energy deposition and overall performance of the fs-ns laser pulses in creating and sustaining laser plasmas. Preliminary work on temporal delay and shaping of the ns-laser heating pulse was presented earlier¹⁷. For consistent comparison of the second ns pulse's performance following preionization from the fs pulse, various metrics such as a peak electron density and a plasma decay time can be considered. However, the strong dependence of the electron density on the time delay between pulses and the laser intensity complicates the establishment of a universal comparison metric. We propose the electron density averaged over a sufficiently long period of time, $\tau \approx 50 \text{ ns} > \Delta t$ as the metric for current analysis. This metric accounts for both the peak electron density and the decay timescale. Furthermore, temporal integration of the electron density reflects energy absorption, as fast gas heating processes, such as electron impact dissociation and dissociative recombination, scale linearly with electron density. Additionally, the peak gas temperature after the heating pulse serves as a direct measure of energy absorption, analogous to the average electron density. In simulations both laser beams are Gaussian in time, the initial pre-ionized channel is created by the fs pulse, with an electron density of $n_e = 10^{23} \text{ m}^{-3}$ and $T_e = 3 \text{ eV}$ in dry air. The ns heating pulse is a 1064 nm wavelength laser with a 10 ns pulse-width.

The simulation results for the average electron density, $\langle n_e \rangle = \tau^{-1} \int_0^\tau n_e(t) dt$, and peak gas temperature for various time delays between fs and the ns pulses at different intensities of the ns pulse are presented in Fig. 22. We observe that the higher laser intensities result in higher average electron density and stronger thermalization. At an intensity of 25 GW/cm^2 , the gas temperature rises from about 300 K to 1300 K due to heating from the second ns laser pulse at the

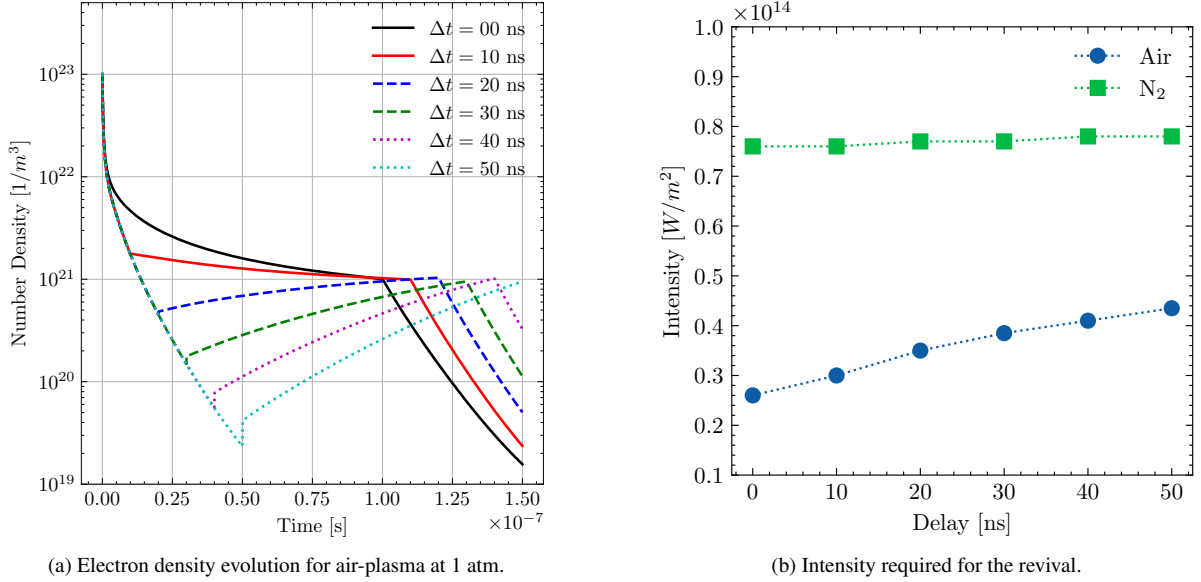


Figure 20. Revival of the electron density to $n_e = 10^{21} \text{ m}^{-3}$ in a dual-pulse laser plasma at various time delays of the second ns heating pulse with a pulse width of 100 ns.

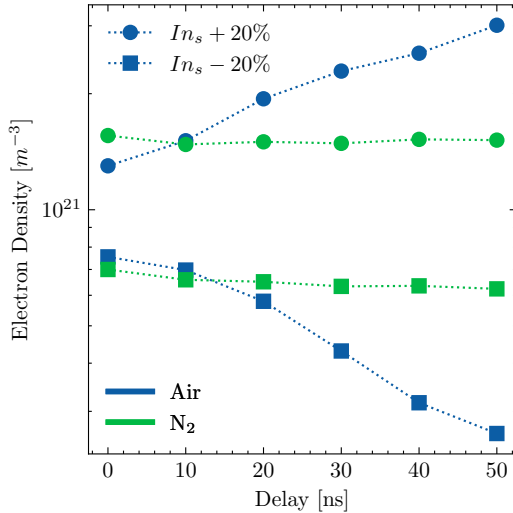


Figure 21. Electron density at the end of the ns-heating pulse (pulse width = 100 ns) with a $\pm 20\%$ variation in the laser intensity, which is required to sustain an electron density of $n_e = 10^{21} \text{ m}^{-3}$ in a dual-pulse laser configuration. The laser intensity required to sustain the electron density is shown in Fig. 20b.

optimal time delay. Using the average electron density as a comparison metric, optimal coupling/pairing occurs around half the pulse width time delay for moderate laser intensities ($I_n > 10^{14} \text{ W/m}^2$). At lower laser intensities ($I_n < 10^{14} \text{ W/m}^2$), optimal pairing shifts to longer time delays between pulses. Similar results were obtained for a nanosecond pulse duration of 16 ns. Consistent with the present findings, earlier experimental work¹⁷ has shown that optimal energy coupling occurs at a positive offset. Photo-detachment is the pri-

mary coupling mechanism at lower laser intensities, with the peak of O_2^- concentration occurring at about 10 ns. The analysis based on thermalization, indicated by the gas temperature, aligns well with the optimal time delay calculated from the proposed metric at moderate laser intensities. However, weak thermalization at lower laser intensities limits the effectiveness of the thermalization-based evaluation of optimal coupling due to the minimal temperature increase.

The advanced capabilities in optics enable the generation of non-Gaussian pulses in time and space. Two shapes, sharp-rise (shape-SR) and sharp-fall (shape-SF), in time are considered for the ns heating pulse to evaluate effects of temporal shaping of the pulse. The non-Gaussian pulse shape is represented by Eq. 9, normalized by the maximum amplitude and the pulse width to keep the same energy as the Gaussian laser pulse for accurate comparison.

$$I_L(t) = \tilde{A} \frac{1}{2} \left(1 - \beta \tanh \left(\frac{t - D - \beta \varepsilon}{\tau_f} \right) \right) \cdot \exp \left(-\frac{1}{2} \left(\frac{t - D - \beta \varepsilon}{\tau_s} \right)^2 \right), \quad \beta \in \{-1, 1\} \quad (9)$$

Here, β represents the shape parameter, D is the time delay, ε denotes a temporal shift, τ_f is the fast time constant, τ_s is the slow time constant, and \tilde{A} is the normalized laser amplitude. In this case, $\varepsilon = 2 \text{ ns}$ and $\tau_f = 1 \text{ ns}$, with other parameters scaled to ensure same energy as the Gaussian pulse. The profiles of these pulses are shown in Fig. 23. The time delay is defined as the time difference between the fs pulse and the peak of the shaped pulse.

For analysis, the plasma generated by the fs pulse is maintained at 0 ns while the second ns pulse is applied with the

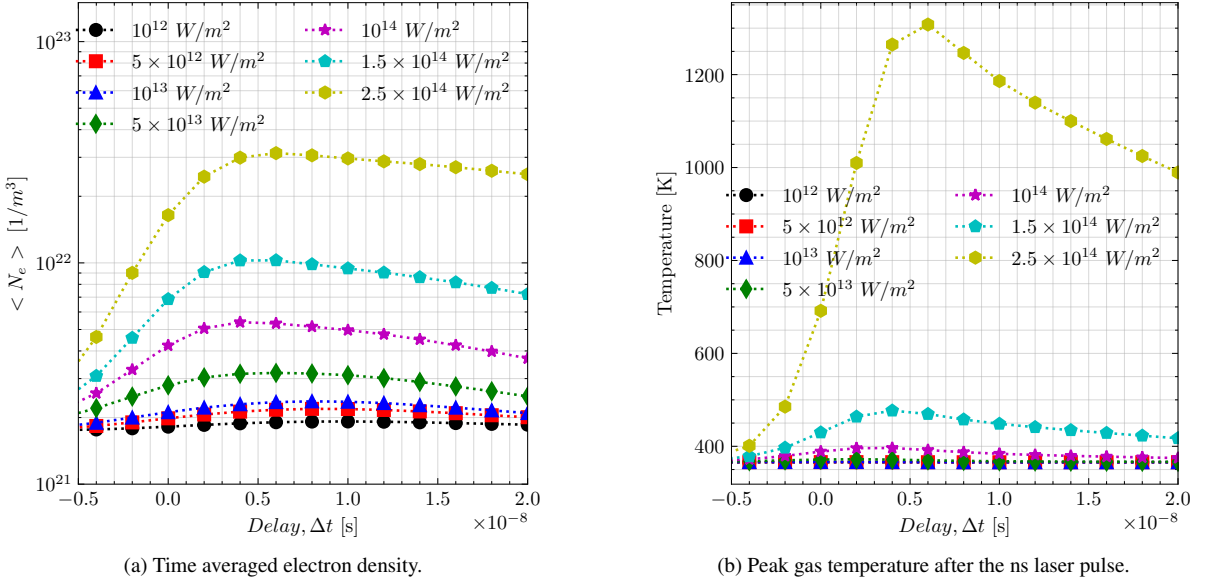


Figure 22. Plasma revival for a range of intensities of the ns laser pulse: the average electron density (left) and gas temperature (right) for a range of time delays between pulses.

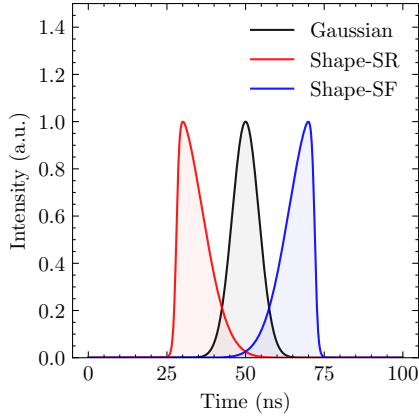


Figure 23. Various temporal shapes of the nanosecond laser pulse.

time delay ranging from -20 ns to 20 ns to evaluate the performance metric. The time-averaged electron density and bulk gas temperature are shown in Fig. 24 for different laser intensities of the ns-laser pulse. Optimal coupling occurs when the electron decay profile closely correlates with the temporal profile of the ns-laser intensity, as absorption is directly proportional to the product of the electron density and laser intensity. Consequently, the laser intensity shape-SR outperforms other pulses due to its stronger correlation with the electron decay curve. The laser intensity shape-SR is preferable for the short time delay between pulses, while the shape-SF is favored for the longer time delay, with the Gaussian pulse performing better in intermediate scenarios. Moreover, for the longer time delays, the earlier tail of the shape-SF pulse experiences higher electron density regions, explaining the improved performance even for longer time delay between pulses. Thus,

the shaped laser pulses demonstrate enhanced performance at corresponding optimal temporal delay conditions compared to the Gaussian.

IV. CONCLUSIONS

The properties of laser-induced plasma have been extensively studied for applications in engineering, manufacturing, diagnostics, and defense. Accurate and reliable methodologies and models are essential for bridging the gap between laboratory studies and real-world applications. However, understanding the underlying physics and developing predictive models for quantitative comparisons remain significant challenges. While recent experimental efforts have explored additional parameters, computational studies providing detailed analyses of the temporal and spatial dynamics of various species and temperatures remain limited.

This work extends a previously developed N_2 plasma kinetics model to enable detailed modeling of non-equilibrium laser plasmas in N_2 - O_2 mixtures. Using a self-consistent approach, the model incorporates enhanced kinetics, including associative ionization and energy coupling mechanisms such as avalanche ionization and photodetachment. It is integrated with the multidimensional plasma solver LOTASFOAM³⁶. Simulation results are compared with available experimental data from the literature, showing reasonable agreement in electron dynamics, gas temperature, and refractive index.

After model validation, the plasma dynamics of fs-laser-induced filaments in atmospheric-pressure air are examined and compared with laser plasmas in pure nitrogen. Quantitative characteristics of plasma properties for fs-laser filament dynamics are provided, covering a range of initial electron densities and electron temperatures. Additionally, fs-ns dual-

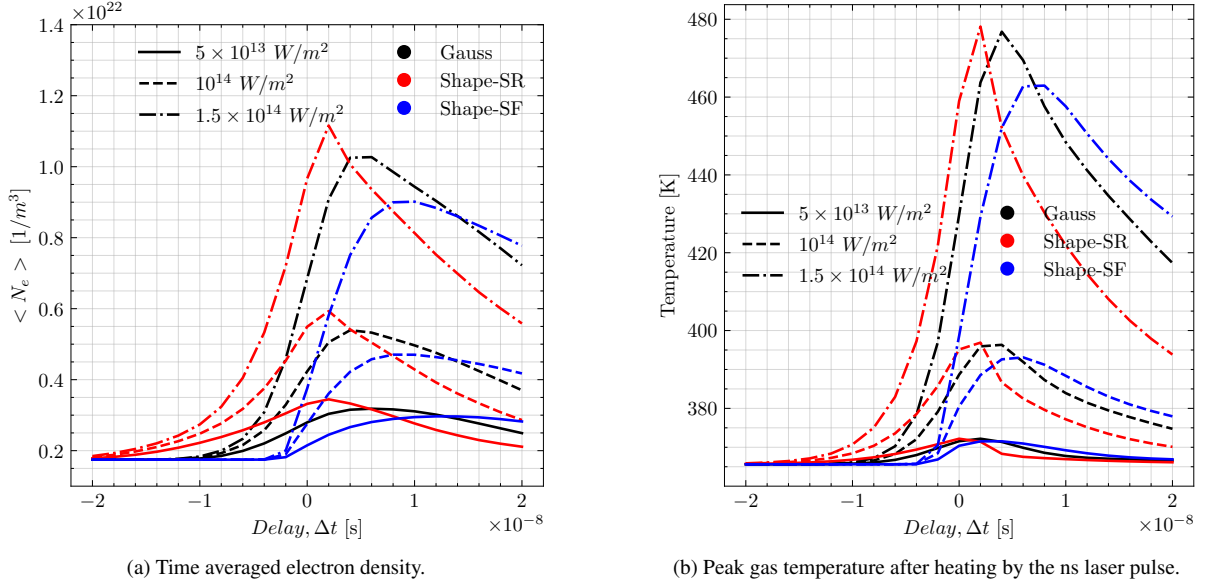


Figure 24. Comparison of performance for temporally shaped ns laser pulses in dual-pulse configuration: the average electron density (left) and gas temperature (right) against time delay between pulses at various laser intensities of the shaped nanosecond pulse (shapes shown in Eq. 9).

pulse laser plasma properties are studied to understand and optimize the energy coupling of the heating ns-laser pulse to the fs-laser filament. Additional experimental measurements of vibrational temperatures, atomic species concentrations, and gas temperature dynamics would be valuable for comparison with the computational results and for enhancing the understanding of non-equilibrium plasmas and their interaction with laser pulses. The main findings are summarized as follows: a) A small addition of O_2 to the nitrogen-oxygen mixture results in a slower decay of electron density; b) In air plasma, the key difference compared to plasma decay in pure nitrogen is the suppression of the N_4^+ production and recombination channel at early times due to the presence of O_2 ; c) An accumulation of negatively charged O_2^- ions is observed at the radial edges of the plasma channel; d) A comparison of single ns-pulse and dual-pulse (fs-ns) plasma reveals improved decay characteristics and reduced sensitivity to small variations in laser parameters, enabling repeatable revival of plasma to an electron density of $n_e = 10^{21} \text{ m}^{-3}$; e) Associative ionization and detachment are key kinetic channels that influence temporal plasma dynamics following the ns-heating pulse in dual-pulse scenarios; f) Optimal energy coupling between the fs-laser filament and heating ns-laser pulse occurs at the delay of half the pulse width for Gaussian pulses; g) In fs-ns dual pulse, the shaped ns pulses outperform Gaussian

pulses at specific time windows.

ACKNOWLEDGMENTS

This work was supported by the Office of Naval Research under grant N00014-22-1-2235 (Program Manager, Mr. Quentin Saulter). The author, S.P., would like to thank Dr. Richard Miles and Dr. Arthur Dogariu for their valuable discussions. A portion of this research was carried out using the advanced computing resources of TERRA and GRACE clusters provided by Texas A&M High-Performance Research Computing.

DATA AVAILABILITY STATEMENT

The data that support the findings of this study are available from the corresponding author upon reasonable request.

Appendix: Reaction Sets

Table IV: Plasma kinetics model for N_2 - O_2 .

ID	Reaction	Rate Expression	Units	References
R1	$2N + N_2 \rightarrow N_2 + N_2(A)$	$1.7 \cdot 10^{-33} \cdot 10^{-12}$	$m^6 s^{-1}$	42,51
R2	$2N + O_2 \rightarrow N_2(A) + O_2$	$1.7 \cdot 10^{-33} \cdot 10^{-12}$	$m^6 s^{-1}$	42,51
R3	$2N + NO \rightarrow N_2(A) + NO$	$1.7 \cdot 10^{-33} \cdot 10^{-12}$	$m^6 s^{-1}$	42,51

Table IV: (Continued)

ID	Reaction	Rate Expression	Units	References
R4	$3N \rightarrow N + N_2(A)$	$10^{-32} \cdot 10^{-12}$	$m^6 s^{-1}$	42,51
R5	$2N + O \rightarrow N_2(A) + O$	$10^{-32} \cdot 10^{-12}$	$m^6 s^{-1}$	42,51
R6	$2N + N_2 \rightarrow N_2 + N_2(B)$	$2.4 \cdot 10^{-33} \cdot 10^{-12}$	$m^6 s^{-1}$	42,51
R7	$2N + O_2 \rightarrow N_2(B) + O_2$	$2.4 \cdot 10^{-33} \cdot 10^{-12}$	$m^6 s^{-1}$	42,51
R8	$2N + NO \rightarrow N_2(B) + NO$	$2.4 \cdot 10^{-33} \cdot 10^{-12}$	$m^6 s^{-1}$	42,51
R9	$3N \rightarrow N + N_2(B)$	$1.4 \cdot 10^{-32} \cdot 10^{-12}$	$m^6 s^{-1}$	42,51
R10	$2N + O \rightarrow N_2(B) + O$	$1.4 \cdot 10^{-32} \cdot 10^{-12}$	$m^6 s^{-1}$	42,51
R11	$N_2(A) \rightarrow N_2 + h\nu$	0.5	s^{-1}	35,41,46
R12	$N_2(B) \rightarrow N_2(A) + h\nu$	152000.0	s^{-1}	35,41,46
R13	$N_2(C) \rightarrow N_2(B) + h\nu$	26900000.0	s^{-1}	35,41,46
R14	$2N_2(A) \rightarrow N_2(v) + N_2(B)$	$2.9 \cdot 10^{-15} \sqrt{\frac{T}{300}}$	$m^3 s^{-1}$	35,41,46
R15	$2N_2(A) \rightarrow N_2(v) + N_2(C)$	$2.6 \cdot 10^{-16} \sqrt{\frac{T}{300}}$	$m^3 s^{-1}$	35,41,46
R16	$N_4^+ + e^- \rightarrow N_2 + N_2(A)$	$0.02 \cdot 1.4 \cdot 10^{-12} \left(\frac{300.0}{T_e}\right)^{0.41}$	$m^3 s^{-1}$	35,41,46
R17	$N_4^+ + e^- \rightarrow N_2 + N_2(B)$	$0.87 \cdot 1.4 \cdot 10^{-12} \left(\frac{300.0}{T_e}\right)^{0.41}$	$m^3 s^{-1}$	35,41,46
R18	$N_4^+ + e^- \rightarrow N_2 + N_2(C)$	$0.11 \cdot 1.4 \cdot 10^{-12} \left(\frac{300.0}{T_e}\right)^{0.41}$	$m^3 s^{-1}$	35,41,46
R19	$N_4^+ + 2e^- \rightarrow 2N_2 + e^-$	$7.0 \cdot 10^{-32} \left(\frac{300}{T_e}\right)^{4.5}$	$m^6 s^{-1}$	35,41,46
R20	$N_3^+ + e^- \rightarrow N + N_2$	$2.0 \cdot 10^{-13} \sqrt{\frac{300}{T_e}}$	$m^3 s^{-1}$	35,41,46
R21	$N_2^+ + e^- \rightarrow N + N(D)$	$1.8 \cdot 10^{-13} \left(\frac{300.0}{T_e}\right)^{0.39} \cdot 0.46$	$m^3 s^{-1}$	35,41,46
R22	$N_2^+ + e^- \rightarrow 2N(D)$	$1.8 \cdot 10^{-13} \left(\frac{300.0}{T_e}\right)^{0.39} \cdot 0.46$	$m^3 s^{-1}$	35,41,46
R23	$N_2^+ + e^- \rightarrow N + N(P)$	$1.8 \cdot 10^{-13} \left(\frac{300.0}{T_e}\right)^{0.39} \cdot 0.08$	$m^3 s^{-1}$	35,41,46
R24	$N_2^+ + e^- \rightarrow N_2 + h\nu$	$4.0 \cdot 10^{-18} \left(\frac{300}{T_e}\right)^{0.7}$	$m^3 s^{-1}$	35,41,46
R25	$N_2 + N_2^+ + e^- \rightarrow 2N_2$	$6.0 \cdot 10^{-39} \left(\frac{300}{T_e}\right)^{1.5}$	$m^6 s^{-1}$	35,41,46
R26	$N_2^+ + 2e^- \rightarrow N_2 + e^-$	$2.0 \cdot 10^{-31} \left(\frac{300}{T_e}\right)^{4.5}$	$m^6 s^{-1}$	35,41,46
R27	$N_2 + e^- \rightarrow N_2^+ + 2e^-$	$\frac{5.05 \cdot 10^{-17} (\sqrt{T_e} + 1.1 \cdot 10^{-5} T_e^{1.5})}{e^{\frac{182000.0}{T_e}}}$	$m^3 s^{-1}$	35,41,46
R28	$N^+ + e^- \rightarrow N$	$3.5 \cdot 10^{-18} \left(\frac{300}{T_e}\right)^{0.7}$	$m^3 s^{-1}$	35,41,46
R29	$N_2 + N^+ + e^- \rightarrow N + N_2$	$6.0 \cdot 10^{-39} \left(\frac{300}{T_e}\right)^{1.5}$	$m^6 s^{-1}$	35,41,46
R30	$N^+ + 2e^- \rightarrow N + e^-$	$2.0 \cdot 10^{-31} \left(\frac{300}{T_e}\right)^{4.5}$	$m^6 s^{-1}$	35,41,46
R31	$N_2(A) + N_3^+ \rightarrow 2N_2 + N^+$	$6.0 \cdot 10^{-16}$	$m^3 s^{-1}$	35,41,46
R32	$N_2(A) + N_2^+ \rightarrow N + N_3^+$	$3.0 \cdot 10^{-16}$	$m^3 s^{-1}$	35,41,46
R33	$N_2(A) + N_2^+ \rightarrow N + N_2 + N^+$	$4.0 \cdot 10^{-16}$	$m^3 s^{-1}$	35,41,46
R34	$N_2 + N_2(A) \rightarrow 2N_2$	$2.0 \cdot 10^{-23}$	$m^3 s^{-1}$	35,41,46
R35	$N + N_2(A) \rightarrow N + N_2$	$6.2 \cdot 10^{-17} \left(\frac{300}{T}\right)^{2/3}$	$m^3 s^{-1}$	35,41,46
R36	$N_2(v) + N_2(B) \rightarrow N_2(v) + N_2(A)$	$1.2 \cdot 10^{-17}$	$m^3 s^{-1}$	35,41,46
R37	$N_2(v) + N_2(C) \rightarrow N_2(v) + N_2(B)$	$1.2 \cdot 10^{-17} \left(\frac{300}{T}\right)^{0.33}$	$m^3 s^{-1}$	35,41,46
R38	$N_2 + N_4^+ \rightarrow 2N_2 + N_2^+$	$2.1 \cdot 10^{-22} e^{\frac{T}{121}}$	$m^3 s^{-1}$	35,41,46
R39	$N + N_4^+ \rightarrow 2N_2 + N^+$	10^{-17}	$m^3 s^{-1}$	35,41,46
R40	$N + N_4^+ \rightarrow N_2 + N_3^+$	10^{-15}	$m^3 s^{-1}$	35,41,46
R41	$N + N_3^+ \rightarrow N_2 + N_2^+$	$6.6 \cdot 10^{-17}$	$m^3 s^{-1}$	35,41,46
R42	$N_2 + N_3^+ \rightarrow 2N_2 + N^+$	$6.0 \cdot 10^{-16}$	$m^3 s^{-1}$	35,41,46
R43	$N_2 + N_2^+ \rightarrow N + N_2 + N^+$	$1.2 \cdot 10^{-17}$	$m^3 s^{-1}$	35,41,46
R44	$N_2 + N_2^+ \rightarrow N + N_3^+$	$5.5 \cdot 10^{-18}$	$m^3 s^{-1}$	35,41,46
R45	$N + N_2^+ \rightarrow N_2 + N^+$	$7.2 \cdot 10^{-19} e^{\frac{300}{T}}$	$m^3 s^{-1}$	35,41,46
R46	$2N_2 + N_2^+ \rightarrow N_4^+ + N_2$	$4.086 \cdot 10^{-42} \cdot \left(8.16e^{\frac{-T}{224}} + 1.1e^{\frac{-T}{997}}\right)$	$m^6 s^{-1}$	35,41,46,52,53
R47	$N + N_2 + N_2^+ \rightarrow N_2 + N_3^+$	$9.0 \cdot 10^{-42} e^{\frac{400}{T}}$	$m^6 s^{-1}$	35,41,46
R48	$N_2 + N^+ \rightarrow N + N_2^+$	10^{-19}	$m^3 s^{-1}$	35,41,46

Table IV: (Continued)

ID	Reaction	Rate Expression	Units	References
R49	$2N_2 + N^+ \rightarrow N_2 + N_3^+$	$2.0 \cdot 10^{-41} \left(\frac{300}{T}\right)^{2.0}$	$m^6 s^{-1}$	35,41,46
R50	$N + N_2 + N^+ \rightarrow N_2 + N_2^+$	$10^{-41} \cdot 300 \cdot \frac{1}{T}$	$m^6 s^{-1}$	35,41,46
R51	$N_2 + e^- \rightarrow N + N(D) + e^-$	$10^{-6} \cdot 4.95 \cdot 10^{-8} \left(\frac{T_e}{6000.0}\right)^{0.388} e^{-\frac{113729.0}{T_e}}$	$m^3 s^{-1}$	35,41,46,54-56
R52	$N + N_2(A) \rightarrow N_2 + N(P)$	$10^{-6} \cdot 5.0 \cdot 10^{-11}$	$m^3 s^{-1}$	35,40,41,46-48
R53	$N_2 + e^- \rightarrow N_2(A, v=0-4) + e^-$	BOLSIG	$m^3 s^{-1}$	68
R54	$N_2(A, v=0-4) + e^- \rightarrow N_2 + e^-$	BOLSIG	$m^3 s^{-1}$	68
R55	$N_2 + e^- \rightarrow N_2(A, v=5-9) + e^-$	BOLSIG	$m^3 s^{-1}$	68
R56	$N_2(A, v=5-9) + e^- \rightarrow N_2 + e^-$	BOLSIG	$m^3 s^{-1}$	68
R57	$N_2 + e^- \rightarrow N_2(B) + e^-$	BOLSIG	$m^3 s^{-1}$	68
R58	$N_2(B) + e^- \rightarrow N_2 + e^-$	BOLSIG	$m^3 s^{-1}$	68
R59	$N_2 + e^- \rightarrow N_2(A, v > 9) + e^-$	BOLSIG	$m^3 s^{-1}$	68
R60	$N_2(A, v > 9) + e^- \rightarrow N_2 + e^-$	BOLSIG	$m^3 s^{-1}$	68
R61	$N_2 + e^- \rightarrow N_2(C) + e^-$	BOLSIG	$m^3 s^{-1}$	68
R62	$N_2(C) + e^- \rightarrow N_2 + e^-$	BOLSIG	$m^3 s^{-1}$	68
R63	$N_2 + N_2(a') \rightarrow N_2 + N_2(B)$	$2.8 \cdot 10^{-13} \cdot 10^{-6}$	$m^3 s^{-1}$	35,41,46,57
R64	$N_2(a') + O_2 \rightarrow N_2 + O + O(D)$	$2.8 \cdot 10^{-11} \cdot 10^{-6}$	$m^3 s^{-1}$	35,41,46,57
R65	$N_2 + e^- \rightarrow N_2(a') + e^-$	BOLSIG	$m^3 s^{-1}$	68
R66	$O_2 + e^- \rightarrow O_2^+ + 2e^-$	BOLSIG	$m^3 s^{-1}$	68
R67	$N_2(A) + N_2(a') \rightarrow N_4^+ + e^-$	$1.5 \cdot 10^{-13} \cdot 10^{-6}$	$m^3 s^{-1}$	35,41,46
R68	$2N_2(a') \rightarrow N_4^+ + e^-$	$3.0 \cdot 10^{-13} \cdot 10^{-6}$	$m^3 s^{-1}$	35,41,46
R69	$O_2^+ + e^- \rightarrow 2O$	$1.95 \cdot 10^{-13} \left(\frac{300.0}{T_e}\right)^{0.7}$	$m^3 s^{-1}$	5,39,50,60,61
R70	$O_4^+ + e^- \rightarrow 2O_2$	$4.2 \cdot 10^{-12} \left(\frac{300.0}{T_e}\right)^{0.5}$	$m^3 s^{-1}$	5,39,50,60,61
R71	$NO^+ + e^- \rightarrow N + O$	$4.0 \cdot 10^{-13} \left(\frac{300.0}{T_e}\right)^{1.5}$	$m^3 s^{-1}$	5,39,50,60,61
R72	$O_2^+ + 2e^- \rightarrow 2O + e^-$	$2.0 \cdot 10^{-19} \left(\frac{T_e}{300.0}\right)^{-4.5} \cdot 10^{-12}$	$m^6 s^{-1}$	50,60,61
R73	$O^+ + 2e^- \rightarrow O + e^-$	$1.4 \cdot 10^{-8} T_e^{-4.5} \cdot 10^{-12}$	$m^6 s^{-1}$	58
R74	$O_2 + O_2^+ + e^- \rightarrow 2O_2$	$3.1 \cdot 10^{-23} T_e^{-1.5} \cdot 10^{-12}$	$m^6 s^{-1}$	58
R75	$N_2 + O_2^+ + e^- \rightarrow N_2 + O_2$	$3.1 \cdot 10^{-23} T_e^{-1.5} \cdot 10^{-12}$	$m^6 s^{-1}$	58
R76	$N_2^+ + O_2 + e^- \rightarrow N_2 + O_2$	$3.1 \cdot 10^{-23} T_e^{-1.5} \cdot 10^{-12}$	$m^6 s^{-1}$	58
R77	$N_2 + O^+ + e^- \rightarrow N_2 + O$	$3.1 \cdot 10^{-23} T_e^{-1.5} \cdot 10^{-12}$	$m^6 s^{-1}$	58
R78	$O_2 + O^+ + e^- \rightarrow O + O_2$	$3.1 \cdot 10^{-23} T_e^{-1.5} \cdot 10^{-12}$	$m^6 s^{-1}$	58
R79	$2O_2 + e^- \rightarrow O_2 + O_2^-$	$1.4 \cdot 10^{-41} \cdot 300 \cdot \frac{1}{T_e} e^{-\frac{600}{T}} e^{\frac{700(-T+T_e)}{TT_e}}$	$m^6 s^{-1}$	5
R80	$N_2 + O_2 + e^- \rightarrow N_2 + O_2^-$	$1.07 \cdot 10^{-43} \cdot 300 \cdot \frac{1}{T_e} e^{-\frac{70}{T}} e^{\frac{1500(-T+T_e)}{TT_e}}$	$m^6 s^{-1}$	5
R81	$O + O_2 + e^- \rightarrow O + O_2^-$	10^{-43}	$m^6 s^{-1}$	5
R82	$O + O_2 + e^- \rightarrow O_2 + O^-$	10^{-43}	$m^6 s^{-1}$	5
R83	$O_3 + e^- \rightarrow O + O_2^-$	$1.92 \cdot 10^{-9} \left(\frac{T_e}{11600}\right)^{-1.5} e^{(-1.3)11600 \cdot \frac{1}{T_e}} 10^{-6}$	$m^3 s^{-1}$	5,63
R84	$O_3 + e^- \rightarrow O_2 + O^-$	$5.87 \cdot 10^{-9} \left(\frac{T_e}{11600}\right)^{-1.5} e^{(-1.59)11600 \cdot \frac{1}{T_e}} 10^{-6}$	$m^3 s^{-1}$	5,63
R85	$N_2 + O_2^- \rightarrow N_2 + O_2 + e^-$	$10^{-6} \cdot 1.9 \cdot 10^{-12} \left(\frac{T}{300}\right)^{0.5} e^{-\frac{4990.0}{T}}$	$m^3 s^{-1}$	39
R86	$O_2 + O_2^- \rightarrow 2O_2 + e^-$	$10^{-6} \cdot 2.7 \cdot 10^{-10} \left(\frac{T}{300}\right)^{0.5} e^{-\frac{5590.0}{T}}$	$m^3 s^{-1}$	39
R87	$N_2(A) + O_2^- \rightarrow N_2 + O_2 + e^-$	$10^{-6} \cdot 2.1 \cdot 10^{-9}$	$m^3 s^{-1}$	39
R88	$N_2(B) + O_2^- \rightarrow N_2 + O_2 + e^-$	$10^{-6} \cdot 2.5 \cdot 10^{-9}$	$m^3 s^{-1}$	39
R89	$N_2(A) + O^- \rightarrow N_2 + O + e^-$	$10^{-6} \cdot 2.2 \cdot 10^{-9}$	$m^3 s^{-1}$	39
R90	$N_2(B) + O^- \rightarrow N_2 + O + e^-$	$10^{-6} \cdot 1.9 \cdot 10^{-9}$	$m^3 s^{-1}$	39
R91	$O + O_2^- \rightarrow O_3 + e^-$	$10^{-6} \cdot 1.5 \cdot 10^{-10}$	$m^3 s^{-1}$	39
R92	$N + O^- \rightarrow NO + e^-$	$10^{-6} \cdot 2.6 \cdot 10^{-10}$	$m^3 s^{-1}$	39
R93	$O_2 + O^- \rightarrow O_3 + e^-$	$10^{-6} \cdot 5.0 \cdot 10^{-15}$	$m^3 s^{-1}$	39
R94	$N_2(A) + O_2 \rightarrow N_2 + 2O$	$1.7 \cdot 10^{-12} \cdot 10^{-6}$	$m^3 s^{-1}$	40,47,48,58
R95	$N_2(A) + O_2 \rightarrow N_2 + O_2$	$7.5 \cdot 10^{-13} \cdot 10^{-6}$	$m^3 s^{-1}$	40,47,48,58
R96	$N_2(A) + O \rightarrow N_2 + O(D)$	$3.0 \cdot 10^{-11} \cdot 10^{-6}$	$m^3 s^{-1}$	40,47,48,58
R97	$N_2(A) + NO \rightarrow N_2 + NO$	$2.1 \cdot 10^{-11} \cdot 10^{-6}$	$m^3 s^{-1}$	40,47,48,58
R98	$N_2(A) + O \rightarrow N + NO$	$7.0 \cdot 10^{-12} \cdot 10^{-6}$	$m^3 s^{-1}$	40,47,48,58
R99	$N_2(B) + O_2 \rightarrow N_2 + 2O$	$3.0 \cdot 10^{-10} \cdot 10^{-6}$	$m^3 s^{-1}$	40,47,48,58

Table IV: (Continued)

ID	Reaction	Rate Expression	Units	References
R100	$N_2(B) + NO \rightarrow N_2(A) + NO$	$2.4 \cdot 10^{-10} \cdot 10^{-6}$	$m^3 s^{-1}$	40,47,48,58
R101	$N_2(C) + O_2 \rightarrow N_2 + O + O(D)$	$2.5 \cdot 10^{-10} \cdot 10^{-6}$	$m^3 s^{-1}$	40,47,48,58
R102	$O_2 + O(D) \rightarrow O + O_2$	$6.4 \cdot 10^{-12} e^{\frac{67.0}{T}} 10^{-6}$	$m^3 s^{-1}$	42,51
R103	$N_2 + O(D) \rightarrow N_2 + O$	$2.3 \cdot 10^{-11} \cdot 10^{-6}$	$m^3 s^{-1}$	42,51
R104	$O + O(D) \rightarrow 2O$	$8.0 \cdot 10^{-12} \cdot 10^{-6}$	$m^3 s^{-1}$	42,51
R105	$O_3 + O(D) \rightarrow 2O + O_2$	$1.2 \cdot 10^{-10} \cdot 10^{-6}$	$m^3 s^{-1}$	42,51
R106	$O_3 + O(D) \rightarrow 2O_2$	$1.2 \cdot 10^{-10} \cdot 10^{-6}$	$m^3 s^{-1}$	42,51
R107	$NO + O(D) \rightarrow N + O_2$	$1.7 \cdot 10^{-10} \cdot 10^{-6}$	$m^3 s^{-1}$	42,51
R108	$O + O_2^- \rightarrow O_2 + O^-$	$10^{-6} \cdot 3.3 \cdot 10^{-10}$	$m^3 s^{-1}$	39
R109	$O_2 + O^- \rightarrow O + O_2^-$	$10^{-6} \cdot 10^{-10}$	$m^3 s^{-1}$	39
R110	$N_4^+ + O_2 \rightarrow 2N_2 + O_2^+$	$10^{-6} \cdot 2.5 \cdot 10^{-10}$	$m^3 s^{-1}$	39
R111	$N_2^+ + O_2 \rightarrow N_2 + O_2^+$	$10^{-6} \cdot 6.0 \cdot 10^{-11}$	$m^3 s^{-1}$	39
R112	$2O_2 + O_2^+ \rightarrow O_2 + O_4^+$	$2.4 \cdot 10^{-30} \left(\frac{300.0}{T}\right)^{3.2} \cdot 10^{-12}$	$m^6 s^{-1}$	39
R113	$N_2 + O_2 + O_2^+ \rightarrow N_2 + O_4^+$	$3.3 \cdot 10^{-35} T^{-3.2} \cdot 10^{-12}$	$m^6 s^{-1}$	39
R114	$N_2 + N_2^+ + O_2 \rightarrow N_4^+ + O_2$	$5.0 \cdot 10^{-29} \cdot 10^{-12}$	$m^6 s^{-1}$	39
R115	$N_2 + O_4^+ \rightarrow N_2 + O_2 + O_2^+$	$3.3 \cdot 10^{-12} \left(\frac{300.0}{T}\right)^{4.0} e^{-\frac{5030.0}{T}}$	$m^3 s^{-1}$	39
R116	$O_2 + O_4^+ \rightarrow 2O_2 + O_2^+$	$3.3 \cdot 10^{-12} \left(\frac{300.0}{T}\right)^{4.0} e^{-\frac{5030.0}{T}}$	$m^3 s^{-1}$	39
R117	$N + O_2 + O^+ \rightarrow NO^+ + O_2$	10^{-41}	$m^6 s^{-1}$	39
R118	$N + N_2 + O^+ \rightarrow N_2 + NO^+$	10^{-41}	$m^6 s^{-1}$	39
R119	$N^+ + O_2 \rightarrow N + O_2^+$	$2.8 \cdot 10^{-16}$	$m^3 s^{-1}$	39
R120	$N^+ + O_2 \rightarrow NO^+ + O$	$2.5 \cdot 10^{-16}$	$m^3 s^{-1}$	39
R121	$N^+ + O \rightarrow N + O^+$	10^{-18}	$m^3 s^{-1}$	39
R122	$N^+ + O_3 \rightarrow NO^+ + O_2$	$5.0 \cdot 10^{-16}$	$m^3 s^{-1}$	39
R123	$NO + N^+ \rightarrow N + NO^+$	$8.0 \cdot 10^{-16}$	$m^3 s^{-1}$	39
R124	$NO + N^+ \rightarrow N_2^+ + O$	$3.0 \cdot 10^{-18}$	$m^3 s^{-1}$	39
R125	$NO + N^+ \rightarrow N_2 + O^+$	10^{-18}	$m^3 s^{-1}$	39
R126	$N_2 + O^+ \rightarrow N + NO^+$	$3.0 \cdot 10^{-18} e^{-0.003117T}$	$m^3 s^{-1}$	39
R127	$N_2^+ + O \rightarrow N + NO^+$	$1.3 \cdot 10^{-10} \left(\frac{300}{T}\right)^{0.5}$	$m^3 s^{-1}$	39
R128	$N_2^+ + O \rightarrow N_2 + O^+$	$10^{-17} \left(\frac{300}{T}\right)^{0.2}$	$m^3 s^{-1}$	39
R129	$N_2^+ + O_3 \rightarrow N_2 + O + O_2^+$	10^{-16}	$m^3 s^{-1}$	39
R130	$N_2^+ + NO \rightarrow N_2 + NO^+$	$3.3 \cdot 10^{-16}$	$m^3 s^{-1}$	39
R131	$N_2 + O_2^+ \rightarrow NO + NO^+$	10^{-23}	$m^3 s^{-1}$	39
R132	$N + O_2^+ \rightarrow NO^+ + O$	$1.2 \cdot 10^{-16}$	$m^3 s^{-1}$	39
R133	$NO + O_2^+ \rightarrow NO^+ + O_2$	$4.4 \cdot 10^{-16}$	$m^3 s^{-1}$	39
R134	$N_4^+ + O \rightarrow 2N_2 + O^+$	$2.5 \cdot 10^{-16}$	$m^3 s^{-1}$	39
R135	$N_4^+ + NO \rightarrow 2N_2 + NO^+$	$4.0 \cdot 10^{-16}$	$m^3 s^{-1}$	39
R136	$O + O_4^+ \rightarrow O_2^+ + O_3$	$3.0 \cdot 10^{-16}$	$m^3 s^{-1}$	39
R137	$NO + O_4^+ \rightarrow NO^+ + 2O_2$	10^{-16}	$m^3 s^{-1}$	39
R138	$O_2 + O_2^- + O_2^+ \rightarrow 2O + 2O_2$	$10^{-12} \cdot 2.0 \cdot 10^{-25} \left(\frac{300}{T}\right)^{2.5}$	$m^6 s^{-1}$	40,47,48
R139	$N_2 + O_2^- + O_2^+ \rightarrow N_2 + 2O + O_2$	$10^{-12} \cdot 2.0 \cdot 10^{-25} \left(\frac{300}{T}\right)^{2.5}$	$m^6 s^{-1}$	40,47,48
R140	$O_2 + O_2^- + O_4^+ \rightarrow 2O + 3O_2$	$10^{-12} \cdot 2.0 \cdot 10^{-25} \left(\frac{300}{T}\right)^{2.5}$	$m^6 s^{-1}$	40,47,48
R141	$N_2 + N_2^+ + O_2^- \rightarrow 2N_2 + O_2$	$2.0 \cdot 10^{-25} \left(\frac{300.0}{T}\right)^{2.5} \cdot 10^{-12}$	$m^6 s^{-1}$	39
R142	$N_2^+ + O_2 + O_2^- \rightarrow N_2 + 2O_2$	$2.0 \cdot 10^{-25} \left(\frac{300.0}{T}\right)^{2.5} \cdot 10^{-12}$	$m^6 s^{-1}$	39
R143	$N_2 + O_2^- + O_2^+ \rightarrow N_2 + 2O_2$	$2.0 \cdot 10^{-25} \left(\frac{300.0}{T}\right)^{2.5} \cdot 10^{-12}$	$m^6 s^{-1}$	39
R144	$O_2 + O_2^- + O_2^+ \rightarrow 3O_2$	$2.0 \cdot 10^{-25} \left(\frac{300.0}{T}\right)^{2.5} \cdot 10^{-12}$	$m^6 s^{-1}$	39
R145	$N_2 + N^+ + O_2^- \rightarrow N + N_2 + O_2$	$2.0 \cdot 10^{-25} \left(\frac{300.0}{T}\right)^{2.5} \cdot 10^{-12}$	$m^6 s^{-1}$	39
R146	$N^+ + O_2 + O_2^- \rightarrow N + 2O_2$	$2.0 \cdot 10^{-25} \left(\frac{300.0}{T}\right)^{2.5} \cdot 10^{-12}$	$m^6 s^{-1}$	39
R147	$N_2 + O_2^- + O^+ \rightarrow N_2 + O + O_2$	$2.0 \cdot 10^{-25} \left(\frac{300.0}{T}\right)^{2.5} \cdot 10^{-12}$	$m^6 s^{-1}$	39
R148	$O_2 + O_2^- + O^+ \rightarrow O + 2O_2$	$2.0 \cdot 10^{-25} \left(\frac{300.0}{T}\right)^{2.5} \cdot 10^{-12}$	$m^6 s^{-1}$	39
R149	$N_2 + NO^+ + O_2^- \rightarrow N_2 + NO + O_2$	$2.0 \cdot 10^{-25} \left(\frac{300.0}{T}\right)^{2.5} \cdot 10^{-12}$	$m^6 s^{-1}$	39
R150	$NO^+ + O_2 + O_2^- \rightarrow NO + 2O_2$	$2.0 \cdot 10^{-25} \left(\frac{300.0}{T}\right)^{2.5} \cdot 10^{-12}$	$m^6 s^{-1}$	39
R151	$N_2 + N_2^+ + O^- \rightarrow 2N_2 + O$	$2.0 \cdot 10^{-25} \left(\frac{300.0}{T}\right)^{2.5} \cdot 10^{-12}$	$m^6 s^{-1}$	39
R152	$N_2^+ + O_2 + O^- \rightarrow N_2 + O + O_2$	$2.0 \cdot 10^{-25} \left(\frac{300.0}{T}\right)^{2.5} \cdot 10^{-12}$	$m^6 s^{-1}$	39

Table IV: (Continued)

ID	Reaction	Rate Expression	Units	References
R153	$N_2 + O_2^+ + O^- \rightarrow N_2 + O + O_2$	$2.0 \cdot 10^{-25} \left(\frac{300.0}{T}\right)^{2.5} \cdot 10^{-12}$	$m^6 s^{-1}$	39
R154	$O_2 + O_2^+ + O^- \rightarrow O + 2O_2$	$2.0 \cdot 10^{-25} \left(\frac{300.0}{T}\right)^{2.5} \cdot 10^{-12}$	$m^6 s^{-1}$	39
R155	$N_2 + N^+ + O^- \rightarrow N + N_2 + O$	$2.0 \cdot 10^{-25} \left(\frac{300.0}{T}\right)^{2.5} \cdot 10^{-12}$	$m^6 s^{-1}$	39
R156	$N^+ + O_2 + O^- \rightarrow N + O + O_2$	$2.0 \cdot 10^{-25} \left(\frac{300.0}{T}\right)^{2.5} \cdot 10^{-12}$	$m^6 s^{-1}$	39
R157	$N_2 + O^- + O^+ \rightarrow N_2 + 2O$	$2.0 \cdot 10^{-25} \left(\frac{300.0}{T}\right)^{2.5} \cdot 10^{-12}$	$m^6 s^{-1}$	39
R158	$O_2 + O^- + O^+ \rightarrow 2O + O_2$	$2.0 \cdot 10^{-25} \left(\frac{300.0}{T}\right)^{2.5} \cdot 10^{-12}$	$m^6 s^{-1}$	39
R159	$N_2 + NO^+ + O^- \rightarrow N_2 + NO + O$	$2.0 \cdot 10^{-25} \left(\frac{300.0}{T}\right)^{2.5} \cdot 10^{-12}$	$m^6 s^{-1}$	39
R160	$NO^+ + O_2 + O^- \rightarrow NO + O + O_2$	$2.0 \cdot 10^{-25} \left(\frac{300.0}{T}\right)^{2.5} \cdot 10^{-12}$	$m^6 s^{-1}$	39
R161	$N_2 + N^+ + O^- \rightarrow N_2 + NO$	$2.0 \cdot 10^{-25} \left(\frac{300.0}{T}\right)^{2.5} \cdot 10^{-12}$	$m^6 s^{-1}$	39
R162	$N^+ + O_2 + O^- \rightarrow NO + O_2$	$2.0 \cdot 10^{-25} \left(\frac{300.0}{T}\right)^{2.5} \cdot 10^{-12}$	$m^6 s^{-1}$	39
R163	$N_2 + O^- + O^+ \rightarrow N_2 + O_2$	$2.0 \cdot 10^{-25} \left(\frac{300.0}{T}\right)^{2.5} \cdot 10^{-12}$	$m^6 s^{-1}$	39
R164	$O_2 + O^- + O^+ \rightarrow 2O_2$	$2.0 \cdot 10^{-25} \left(\frac{300.0}{T}\right)^{2.5} \cdot 10^{-12}$	$m^6 s^{-1}$	39
R165	$N + O_2 \rightarrow NO + O$	$10^{-6} \cdot 1.1 \cdot 10^{-14} T e^{-\frac{3150.0}{T}}$	$m^3 s^{-1}$	39
R166	$N + O_3 \rightarrow NO + O_2$	$10^{-6} \cdot 2.0 \cdot 10^{-16}$	$m^3 s^{-1}$	39
R167	$N + NO \rightarrow N_2 + O$	$10^{-6} \cdot 1.05 \cdot 10^{-12} T^{0.5}$	$m^3 s^{-1}$	39
R168	$O + O_3 \rightarrow 2O_2$	$10^{-6} \cdot 2.0 \cdot 10^{-11} e^{-\frac{2300.0}{T}}$	$m^3 s^{-1}$	39
R169	$2N + O_2 \rightarrow N_2 + O_2$	$0.5 \cdot 10^{-12} \cdot 8.76 \cdot 10^{-34} e^{\frac{500}{T}}$	$m^6 s^{-1}$	39
R170	$N_2 + 2O \rightarrow N_2 + O_2$	$10^{-12} \cdot 2.76 \cdot 10^{-34} e^{\frac{720.0}{T}}$	$m^6 s^{-1}$	39
R171	$2O + O_2 \rightarrow 2O_2$	$10^{-12} \cdot 2.45 \cdot 10^{-31} T^{-0.63}$	$m^6 s^{-1}$	39
R172	$N_2 + O + O_2 \rightarrow N_2 + O_3$	$\frac{5.6 \cdot 10^{-41}}{T^{2.0}}$	$m^6 s^{-1}$	39
R173	$O + 2O_2 \rightarrow O_2 + O_3$	$\frac{8.6 \cdot 10^{-43}}{T^{1.25}}$	$m^6 s^{-1}$	39
R174	$N_2 + O \rightarrow N + NO$	$\frac{1.121 \cdot 10^{-16} e^{-\frac{3.75 \cdot 10^4}{T}}}{T^{1.0}}$	$m^3 s^{-1}$	39
R175	$NO + O \rightarrow N + O_2$	$5.281 \cdot 10^{-21} T e^{-\frac{1.97 \cdot 10^4}{T}}$	$m^3 s^{-1}$	39
R176	$N + N(P) \rightarrow N + N(D)$	$1.8 \cdot 10^{-18}$	$m^3 s^{-1}$	40,47,48
R177	$N(P) + O \rightarrow N(D) + O$	10^{-18}	$m^3 s^{-1}$	40,47,48
R178	$N(P) + O_2 \rightarrow NO + O(D)$	$1.25 \cdot 10^{-18}$	$m^3 s^{-1}$	40,47,48
R179	$N(P) + O_2 \rightarrow NO + O$	$1.25 \cdot 10^{-18}$	$m^3 s^{-1}$	40,47,48
R180	$NO + N(P) \rightarrow N_2 + O(D)$	$1.45 \cdot 10^{-17}$	$m^3 s^{-1}$	40,47,48
R181	$NO + N(P) \rightarrow N_2 + O$	$1.45 \cdot 10^{-17}$	$m^3 s^{-1}$	40,47,48
R182	$N(D) + O_2 \rightarrow NO + O(D)$	$7.3 \cdot 10^{-18} e^{-\frac{185.0}{T^{1.0}}}$	$m^3 s^{-1}$	40,47,48
R183	$N(D) + O_2 \rightarrow NO + O$	$2.4 \cdot 10^{-18} e^{-\frac{185.0}{T^{1.0}}}$	$m^3 s^{-1}$	40,47,48
R184	$N(D) + O \rightarrow N + O$	$1.4 \cdot 10^{-18}$	$m^3 s^{-1}$	40,47,48
R185	$NO + N(D) \rightarrow N_2(v) + O(D)$	$3.96 \cdot 10^{-17}$	$m^3 s^{-1}$	40,47,48
R186	$NO + N(D) \rightarrow N_2(v) + O$	$2.04 \cdot 10^{-17}$	$m^3 s^{-1}$	40,47,48
R187	$N_2 + N(D) \rightarrow N + N_2$	$10^{-19} e^{-\frac{510.0}{T^{1.0}}}$	$m^3 s^{-1}$	40,47,48
R188	$N(D) + N(P) \rightarrow N_2^+ + e^-$	$3.0 \cdot 10^{-22} T^{1.2} e^{\frac{80.0}{T^{1.0}}}$	$m^3 s^{-1}$	40,47,48
R189	$2N(P) \rightarrow N_2^+ + e^-$	$5.796 \cdot 10^{-18} T^{0.1667}$	$m^3 s^{-1}$	40,47,48
R190	$N(P) + O \rightarrow NO^+ + e^-$	$5.796 \cdot 10^{-18} T^{0.1667}$	$m^3 s^{-1}$	40,47,48
R191	$O_2 + e^- \rightarrow 2O + e^-$	$10^{-6} \cdot 10.0 \frac{(0.0005402T_e^{1.178} + 1.777 \cdot 10^{-8} T_e^{2.0} + 8.4)}{(6.501 \cdot 10^{-5} T_e^{1.178} + 2.139 \cdot 10^{-9} T_e^{2.0})^{1.0}}$	$m^3 s^{-1}$	39,58
R192	$O_2 + e^- \rightarrow O + O(D) + e^-$	$10^{-6} \cdot 10.0 \frac{(0.000511T_e^{1.178} + 1.681 \cdot 10^{-8} T_e^{2.0} + 17.2)}{(6.501 \cdot 10^{-5} T_e^{1.178} + 2.139 \cdot 10^{-9} T_e^{2.0})^{1.0}}$	$m^3 s^{-1}$	39,58
R193	$2N_2 \rightarrow 2N + N_2$	$\frac{2.019 \cdot 10^{-10} e^{-\frac{1.132 \cdot 10^5}{(TT_v)^{0.5}}}}{(TT_v)^{0.607}}$	$m^3 s^{-1}$	54–56
R194	$2N + N_2 \rightarrow 2N_2$	$8.27 \cdot 10^{-46} e^{\frac{500.0 - 6.918 \cdot 10^{-7} T^{2.54}}{T^{1.0}}}$	$m^6 s^{-1}$	54–56,59
R195	$N_2 + O_2 \rightarrow 2N + O_2$	$\frac{1.162 \cdot 10^{-8} e^{-\frac{1.132 \cdot 10^5}{(TT_v)^{0.5}}}}{(TT_v)^{0.8}}$	$m^3 s^{-1}$	54–56
R196	$N_2 + NO \rightarrow 2N + NO$	$\frac{1.162 \cdot 10^{-8} e^{-\frac{1.132 \cdot 10^5}{(TT_v)^{0.5}}}}{(TT_v)^{0.8}}$	$m^3 s^{-1}$	54–56
R197	$2N + NO \rightarrow N_2 + NO$	$8.27 \cdot 10^{-46} e^{\frac{500.0 - 6.918 \cdot 10^{-7} T^{2.54}}{T^{1.0}}}$	$m^6 s^{-1}$	54–56

Table IV: (Continued)

ID	Reaction	Rate Expression	Units	References
R198	$N + N_2 \rightarrow 3N$	$\frac{5.963 \cdot 10^{-10} e^{-\frac{1.132 \cdot 10^5}{(T_i)^{0.5}}}}{(T_i)^{0.613}}$	$m^3 s^{-1}$	54–56
R199	$3N \rightarrow N + N_2$	$8.27 \cdot 10^{-46} e^{\frac{500.0 - 6.918 \cdot 10^{-7} T^{2.54}}{T^{1.0}}}$	$m^6 s^{-1}$	54–56
R200	$N_2 + O \rightarrow 2N + O$	$\frac{4.982 \cdot 10^{-8} e^{-\frac{1.132 \cdot 10^5}{(T_i)^{0.5}}}}{(T_i)^{0.8}}$	$m^3 s^{-1}$	54–56
R201	$2N + O \rightarrow N_2 + O$	$8.27 \cdot 10^{-46} e^{\frac{500.0 - 6.918 \cdot 10^{-7} T^{2.54}}{T^{1.0}}}$	$m^6 s^{-1}$	54–56
R202	$N_2 + N_2^+ \rightarrow 2N + N_2^+$	$\frac{2.019 \cdot 10^{-10} e^{-\frac{1.132 \cdot 10^5}{(T_i)^{0.5}}}}{(T_i)^{0.607}}$	$m^3 s^{-1}$	54–56
R203	$2N + N_2^+ \rightarrow N_2 + N_2^+$	$8.27 \cdot 10^{-46} e^{\frac{500.0 - 6.918 \cdot 10^{-7} T^{2.54}}{T^{1.0}}}$	$m^6 s^{-1}$	54–56
R204	$N_2 + O_2^+ \rightarrow 2N + O_2^+$	$\frac{1.162 \cdot 10^{-8} e^{-\frac{1.132 \cdot 10^5}{(T_i)^{0.5}}}}{(T_i)^{0.8}}$	$m^3 s^{-1}$	54–56
R205	$2N + O_2^+ \rightarrow N_2 + O_2^+$	$8.27 \cdot 10^{-46} e^{\frac{500.0 - 6.918 \cdot 10^{-7} T^{2.54}}{T^{1.0}}}$	$m^6 s^{-1}$	54–56
R206	$N_2 + NO^+ \rightarrow 2N + NO^+$	$\frac{1.162 \cdot 10^{-8} e^{-\frac{1.132 \cdot 10^5}{(T_i)^{0.5}}}}{(T_i)^{0.8}}$	$m^3 s^{-1}$	54–56
R207	$N_2 + N^+ \rightarrow 2N + N^+$	$\frac{5.963 \cdot 10^{-10} e^{-\frac{1.132 \cdot 10^5}{(T_i)^{0.5}}}}{(T_i)^{0.613}}$	$m^3 s^{-1}$	54–56
R208	$N_2 + O^+ \rightarrow 2N + O^+$	$\frac{4.982 \cdot 10^{-8} e^{-\frac{1.132 \cdot 10^5}{(T_i)^{0.5}}}}{(T_i)^{0.8}}$	$m^3 s^{-1}$	54–56
R209	$N_2 + O_2 \rightarrow N_2 + 2O$	$\frac{5.57 \cdot 10^{-15} e^{-\frac{5.95 \cdot 10^4}{T^{1.0}}}}{T^{0.2726}}$	$m^3 s^{-1}$	54–56
R210	$2O_2 \rightarrow 2O + O_2$	$\frac{1.855 \cdot 10^{-5} e^{-\frac{5.95 \cdot 10^4}{T^{1.0}}}}{T^{2.385}}$	$m^3 s^{-1}$	54–56
R211	$NO + O_2 \rightarrow NO + 2O$	$\frac{5.57 \cdot 10^{-15} e^{-\frac{5.95 \cdot 10^4}{T^{1.0}}}}{T^{0.2726}}$	$m^3 s^{-1}$	54–56
R212	$NO + 2O \rightarrow NO + O_2$	$\frac{6.332 \cdot 10^{-53} e^{\frac{3310.07 - 0.00015677^{3.0} - 5.237 \cdot 10^5}{T^{2.0}}}}{T^{0.2726} (T - 1.0)^{1.909}}$	$m^6 s^{-1}$	54–56
R213	$N + O_2 \rightarrow N + 2O$	$\frac{1.661 \cdot 10^{-8} e^{-\frac{5.95 \cdot 10^4}{T^{1.0}}}}{T^{1.5}}$	$m^3 s^{-1}$	54–56
R214	$O + O_2 \rightarrow 3O$	$\frac{4.982 \cdot 10^{-9} e^{-\frac{5.95 \cdot 10^4}{T^{1.0}}}}{T^{1.5}}$	$m^3 s^{-1}$	54–56
R215	$3O \rightarrow O + O_2$	$\frac{5.664 \cdot 10^{-47} e^{\frac{3310.07 - 0.00015677^{3.0} - 5.237 \cdot 10^5}{T^{2.0}}}}{T^{1.5} (T - 1.0)^{1.909}}$	$m^6 s^{-1}$	54–56
R216	$N_2^+ + O_2 \rightarrow N_2^+ + 2O$	$\frac{5.57 \cdot 10^{-15} e^{-\frac{5.95 \cdot 10^4}{T^{1.0}}}}{T^{0.2726}}$	$m^3 s^{-1}$	54–56
R217	$O_2 + O_2^+ \rightarrow 2O + O_2^+$	$\frac{1.855 \cdot 10^{-5} e^{-\frac{5.95 \cdot 10^4}{T^{1.0}}}}{T^{2.385}}$	$m^3 s^{-1}$	54–56
R218	$NO^+ + O_2 \rightarrow NO^+ + 2O$	$\frac{5.57 \cdot 10^{-15} e^{-\frac{5.95 \cdot 10^4}{T^{1.0}}}}{T^{0.2726}}$	$m^3 s^{-1}$	54–56
R219	$N^+ + O_2 \rightarrow N^+ + 2O$	$\frac{1.661 \cdot 10^{-8} e^{-\frac{5.95 \cdot 10^4}{T^{1.0}}}}{T^{1.5}}$	$m^3 s^{-1}$	54–56
R220	$O_2 + O^+ \rightarrow 2O + O^+$	$\frac{4.982 \cdot 10^{-9} e^{-\frac{5.95 \cdot 10^4}{T^{1.0}}}}{T^{1.5}}$	$m^3 s^{-1}$	54–56
R221	$N_2 + NO \rightarrow N + N_2 + O$	$2.408 \cdot 10^{-15} e^{-\frac{7.52 \cdot 10^4}{T^{1.0}}}$	$m^3 s^{-1}$	54–56
R222	$N + N_2 + O \rightarrow N_2 + NO$	$\frac{5.76 \cdot 10^{-53} e^{\frac{3520.07 - 0.00020937^{3.0} - 5.586 \cdot 10^5}{T^{2.0}}}}{(T - 1.0)^{2.028}}$	$m^6 s^{-1}$	54–56
R223	$NO + O_2 \rightarrow N + O + O_2$	$2.408 \cdot 10^{-15} e^{-\frac{7.52 \cdot 10^4}{T^{1.0}}}$	$m^3 s^{-1}$	54–56
R224	$N + O + O_2 \rightarrow NO + O_2$	$\frac{5.76 \cdot 10^{-53} e^{\frac{3520.07 - 0.00020937^{3.0} - 5.586 \cdot 10^5}{T^{2.0}}}}{(T - 1.0)^{2.028}}$	$m^6 s^{-1}$	54–56
R225	$2NO \rightarrow N + NO + O$	$1.601 \cdot 10^{-15} e^{-\frac{7.52 \cdot 10^4}{T^{1.0}}}$	$m^3 s^{-1}$	54–56
R226	$N + NO + O \rightarrow 2NO$	$\frac{3.829 \cdot 10^{-53} e^{\frac{3520.07 - 0.00020937^{3.0} - 5.586 \cdot 10^5}{T^{2.0}}}}{(T - 1.0)^{2.028}}$	$m^6 s^{-1}$	54–56
R227	$N + NO \rightarrow 2N + O$	$1.601 \cdot 10^{-15} e^{-\frac{7.52 \cdot 10^4}{T^{1.0}}}$	$m^3 s^{-1}$	54–56
R228	$2N + O \rightarrow N + NO$	$\frac{3.829 \cdot 10^{-53} e^{\frac{3520.07 - 0.00020937^{3.0} - 5.586 \cdot 10^5}{T^{2.0}}}}{(T - 1.0)^{2.028}}$	$m^6 s^{-1}$	54–56
R229	$NO + O \rightarrow N + 2O$	$1.601 \cdot 10^{-15} e^{-\frac{7.52 \cdot 10^4}{T^{1.0}}}$	$m^3 s^{-1}$	54–56

Table IV: (Continued)

ID	Reaction	Rate Expression	Units	References
R230	$N + 2O \rightarrow NO + O$	$\frac{3.829 \cdot 10^{-53} e^{\frac{3520.07 - 0.00020937 \cdot 3.0 - 5.586 \cdot 10^5}{72.0}}}{(T-1.0)^{2.028}}$	$m^6 s^{-1}$	54–56
R231	$N_2^+ + NO \rightarrow N + N_2^+ + O$	$2.408 \cdot 10^{-15} e^{-\frac{7.52 \cdot 10^4}{T1.0}}$	$m^3 s^{-1}$	54–56
R232	$NO + O_2^+ \rightarrow N + O + O_2^+$	$2.408 \cdot 10^{-15} e^{-\frac{7.52 \cdot 10^4}{T1.0}}$	$m^3 s^{-1}$	54–56
R233	$NO + NO^+ \rightarrow N + NO^+ + O$	$1.601 \cdot 10^{-15} e^{-\frac{7.52 \cdot 10^4}{T1.0}}$	$m^3 s^{-1}$	54–56
R234	$NO + N^+ \rightarrow N + N^+ + O$	$1.601 \cdot 10^{-15} e^{-\frac{7.52 \cdot 10^4}{T1.0}}$	$m^3 s^{-1}$	54–56
R235	$NO + O^+ \rightarrow N + O + O^+$	$1.601 \cdot 10^{-15} e^{-\frac{7.52 \cdot 10^4}{T1.0}}$	$m^3 s^{-1}$	54–56
R236	$N_2 + O_2 \rightarrow NO + NO^+ + e^-$	$\frac{2.292 \cdot 10^{-10} e^{-\frac{1.41 \cdot 10^5}{T1.0}}}{T^{1.84}}$	$m^3 s^{-1}$	54–56
R237	$2N \rightarrow N_2^+ + e^-$	$2.7 \cdot 10^{-17} e^{-\frac{6.74 \cdot 10^4}{T1.0}}$	$m^3 s^{-1}$	54–56
R238	$2O \rightarrow O_2^+ + e^-$	$\frac{2.657 \cdot 10^{-13} e^{-\frac{8.08 \cdot 10^4}{T1.0}}}{T^{0.98}}$	$m^3 s^{-1}$	54–56
R239	$N + O \rightarrow NO^+ + e^-$	$1.499 \cdot 10^{-20} T^{0.5} e^{-\frac{3.24 \cdot 10^4}{T1.0}}$	$m^3 s^{-1}$	54–56
R240	$N + e^- \rightarrow N^+ + 2e^-$	$\frac{182.7 e^{-\frac{1.69 \cdot 10^5}{T1.0}}}{T^{3.14}}$	$m^3 s^{-1}$	54–56
R241	$O + e^- \rightarrow O^+ + 2e^-$	$\frac{59.78 e^{-\frac{1.58 \cdot 10^5}{T1.0}}}{T^{2.91}}$	$m^3 s^{-1}$	54–56

REFERENCES

- ¹C. M. Limbach, *Characterization of nanosecond, femtosecond and dual pulse laser energy deposition in air for flow control and diagnostic applications*, Ph.D. thesis, Princeton University (2015).
- ²A. Tropina and M. N. Shneider, “Modeling of laser ignition in hydrogen-air mixture,” (American Institute of Aeronautics and Astronautics (AIAA), 2020).
- ³C. Dumitrache, R. VanOsdol, C. M. Limbach, and A. P. Yalin, “Control of Early Flame Kernel Growth by Multi-Wavelength Laser Pulses for Enhanced Ignition,” *Scientific Reports* **7**, 10239 (2017).
- ⁴C. Dumitrache, C. M. Limbach, and A. P. Yalin, “Laser thermal ignition using a dual-pulse approach,” 54th AIAA Aerospace Sciences Meeting **0** (2016), 10.2514/6.2016-0460.
- ⁵M. N. Shneider, A. M. Zheltikov, and R. B. Miles, “Tailoring the air plasma with a double laser pulse,” *Physics of Plasmas* **18** (2011), 10.1063/1.3601764.
- ⁶F. Barkusky, C. Peth, A. Bayer, and K. Mann, “Direct photo-etching of poly(methyl methacrylate) using focused extreme ultraviolet radiation from a table-top laser-induced plasma source,” *Journal of Applied Physics* **101**, 124908 (2007).
- ⁷N. Jhaji, E. Rosenthal, R. Birnbaum, J. W. P. R. X., and undefined 2014, “Demonstration of long-lived high-power optical waveguides in air,” *APS* **4** (2014), 10.1103/PhysRevX.4.011027, publisher: American Physical Society.
- ⁸M. R. Edwards, A. Dogariu, and R. B. Miles, “Simultaneous temperature and velocity measurements in air with femtosecond laser tagging,” *AIAA Journal* **53**, 2280–2288 (2015), publisher: American Institute of Aeronautics and Astronautics Inc.
- ⁹C. Dumitrache, R. VanOsdol, C. M. Limbach, and A. P. Yalin, “Control of Early Flame Kernel Growth by Multi-Wavelength Laser Pulses for Enhanced Ignition,” *Scientific Reports* **7**, 10239 (2017), number: 1 Publisher: Nature Publishing Group.
- ¹⁰A. P. Yalin, N. Wilvert, C. Dumitrache, S. Joshi, and M. N. Shneider, “Laser plasma formation assisted by ultraviolet pre-ionization,” *Physics of Plasmas* **21**, 103511 (2014).
- ¹¹A. A. Tropina, R. B. Miles, and M. N. Shneider, “Mathematical Model of Dual-Pulse Laser Ignition,” *Journal of Propulsion and Power* (2017), 10.2514/1.b36687.
- ¹²A. A. Tropina, S. Pokharel, M. R. New-Tolley, and M. N. Shneider, “Plasma defocusing in dual-pulse laser ignition,” *Journal of Physics D: Applied Physics* **54**, 225205 (2021), publisher: IOP Publishing.
- ¹³N. L. Aleksandrov, S. B. Bodrov, M. V. Tsarev, A. A. Murzanev, Y. A. Sergeev, Y. A. Malkov, and A. N. Stepanov, “Decay of femtosecond laser-induced plasma filaments in air, nitrogen, and argon for atmospheric and subatmospheric pressures,” *Physical Review E* **94**, 013204 (2016), publisher: American Physical Society.
- ¹⁴Z. Sun, J. Chen, and W. Rudolph, “Determination of the transient electron temperature in a femtosecond-laser-induced air plasma filament,” *Physical Review E* **83**, 046408 (2011), publisher: American Physical Society.
- ¹⁵P. Chizhov, V. Bukin, and S. Garmov, “Interferometry in Femtosecond Laser Plasma Diagnostics,” *Physics Procedia 18th Conference on Plasma-Surface Interactions, PSI 2015, 5-6 February 2015, Moscow, Russian Federation and the 1st Conference on Plasma and Laser Research and Technologies, PLRT 2015, 18-20 February 2015, Moscow, Russian Federation*, **71**, 222–226 (2015).
- ¹⁶“Two-dimensional high resolution electron properties of femtosecond laser-induced plasma filament in atmospheric pressure argon,” (2023).
- ¹⁷J. Bak, S. Pokharel, H. Hadden, A. Naidu, K. T. Ruggles, A. Tropina, and R. Miles, “Laser intensity shaping: Hydrodynamic effects and energy coupling in dual pulse laser energy deposition,” in *AIAA SCITECH 2024 Forum* (American Institute of Aeronautics and Astronautics, Orlando, FL, 2024).
- ¹⁸J. Papeer, D. Gordon, P. Sprangle, M. Botton, and A. Zigler, “Temporal evolution of femtosecond laser induced plasma filament in air and N₂,” *Applied Physics Letters* **103**, 244102 (2013).
- ¹⁹V. P. Blanchard, S. Wilson, C. Dumitrache, and A. P. Yalin, “Characterization of Femtosecond Laser Filaments in Air by Optical Emission Spectroscopy,” in *AIAA AVIATION FORUM AND ASCEND 2024*, AIAA Aviation Forum and ASCEND Co-Located Conference Proceedings (American Institute of Aeronautics and Astronautics, 2024).
- ²⁰J. Papeer, M. Botton, D. Gordon, P. Sprangle, A. Zigler, and Z. Henis, “Extended lifetime of high density plasma filament generated by a dual femtosecond–nanosecond laser pulse in air,” *New Journal of Physics* **16**, 123046 (2014).
- ²¹F. Théberge, W. Liu, P. T. Simard, A. Becker, and S. L. Chin, “Plasma density inside a femtosecond laser filament in air: Strong dependence on external focusing,” *Physical Review E* **74**, 036406 (2006).
- ²²D. Reyes, M. Baudelet, M. Richardson, and S. Rostami Fairchild, “Transition from linear- to nonlinear-focusing regime of laser filament plasma dynamics,” *Journal of Applied Physics* **124**, 053103 (2018).
- ²³X.-L. Liu, X. Lu, X. Liu, T.-T. Xi, F. Liu, J.-L. Ma, and J. Zhang, “Tightly focused femtosecond laser pulse in air: From filamentation to breakdown,”

- Optics Express **18**, 26007–26017 (2010).
- ²⁴P. P. Kiran, “Focal dynamics of multiple filaments: Microscopic imaging and reconstruction,” *Physical Review A* **82** (2010), 10.1103/PhysRevA.82.013805.
 - ²⁵A. Braun, G. Korn, X. Liu, D. Du, J. Squier, and G. Mourou, “Self-channeling of high-peak-power femtosecond laser pulses in air,” *Optics Letters* **20**, 73–75 (1995).
 - ²⁶G. Méchain, A. Couairon, Y.-B. André, C. D’Amico, M. Franco, B. Prade, S. Tzortzakis, A. Mysyrowicz, and R. Sauerbrey, “Long-range self-channeling of infrared laser pulses in air: A new propagation regime without ionization,” *Applied Physics B* **79**, 379–382 (2004).
 - ²⁷V. P. Blanchard, R. Rosser, G. Urdaneta, A. Dogariu, and A. P. Yalin, “Characterization of a Femtosecond Plasma Filament in Air by fs/ps Hybrid Coherent Anti-Stokes Raman Scattering,” in *AIAA SCITECH 2025 Forum* (American Institute of Aeronautics and Astronautics, 2025).
 - ²⁸J. Bak, G. Urdaneta, S. Pokharel, R. B. Miles, and A. Tropina, “Two-dimensional high resolution electron properties of femtosecond laser-induced plasma filament in atmospheric pressure argon,” *Scientific Reports* **14**, 3703 (2024).
 - ²⁹G. Urdaneta, J. Bak, S. Pokharel, A. Tropina, R. B. Miles, and A. Dogariu, “Temporally resolved properties of femtosecond laser-induced plasmas in air,” *Physical Review Applied*, Submitted, Under Review (2025).
 - ³⁰P. Polynkin, M. Scheller, and J. V. Moloney, “Seeded optical breakdown of molecular and noble gases,” *AIP Conference Proceedings* **1464**, 68–78 (2012).
 - ³¹O. G. Kosareva, D. V. Mokrousova, N. A. Panov, I. A. Nikolaeva, D. E. Shipilo, E. V. Mitina, A. V. Koribut, G. E. Rizaev, A. Couairon, A. Houard, A. B. Savel’ev, L. V. Seleznev, A. A. Ionin, and S. L. Chin, “Remote triggering of air-gap discharge by a femtosecond laser filament and postfilamentation at distances up to 80 m,” *Applied Physics Letters* **119**, 041103 (2021).
 - ³²J. Michael, M. Edwards, R. Miles, and A. Dogariu, “Localized microwave plasma grid by laser-designation,” in *42nd AIAA Plasmadynamics and Lasers Conference, Fluid Dynamics and Co-located Conferences* (American Institute of Aeronautics and Astronautics, 2011).
 - ³³Z. Feng, R. Li, W. Li, Y. Liu, X. Shu, C. Yu, J. Li, and X. Liu, “The propagation of femtosecond laser filaments in air with continuously varying pressures,” *Optics Communications* **502**, 127404 (2022).
 - ³⁴A. M. Perelomov, V. S. Popov, and M. V. Terent’ev, “Ionization of Atoms in an Alternating Electric Field,” *Soviet Journal of Experimental and Theoretical Physics* **23**, 924 (1966), aDS Bibcode: 1966JETP...23.924P.
 - ³⁵C. J. Peters, *Considerations for Femtosecond Laser Electronic Excitation Tagging in High-Speed Flows*, Ph.D. thesis (2019), nTRS Author Affiliations: Glenn Research Center NTRS Report/Patent Number: GRC-E-DAA-TN70850 NTRS Document ID: 20190028876 NTRS Research Center: Glenn Research Center (GRC).
 - ³⁶S. Pokharel and A. A. Tropina, “Self-consistent model and numerical approach for laser-induced non-equilibrium plasma,” *Journal of Applied Physics* **134**, 223301 (2023).
 - ³⁷C. H. Kruger, C. O. Laux, L. Yu, D. M. Packan, and L. Pierrot, “Nonequilibrium discharges in air and nitrogen plasmas at atmospheric pressure,” *Pure and Applied Chemistry* **74**, 337–347 (2002), publisher: De Gruyter.
 - ³⁸M. N. Shneider, A. M. Zheltikov, and R. B. Miles, “Tailoring the air plasma with a double laser pulse,” *Physics of Plasmas* **18**, 063509 (2011).
 - ³⁹I. A. Kossyi, A. Y. Kostinsky, A. A. Matveyev, and V. P. Silakov, “Kinetic scheme of the non-equilibrium discharge in nitrogen-oxygen mixtures,” *Plasma Sources Science and Technology* **1**, 207 (1992).
 - ⁴⁰N. A. Popov, “Associative ionization reactions involving excited atoms in nitrogen plasma,” *Plasma Physics Reports* **35**, 436–449 (2009).
 - ⁴¹M. N. Shneider, A. Baltuška, and A. M. Zheltikov, “Population inversion of molecular nitrogen in an Ar: N₂ mixture by selective resonance-enhanced multiphoton ionization,” *Journal of Applied Physics* **110**, 083112 (2011).
 - ⁴²A. Obrusník, P. Bílek, T. Hoder, M. Šimek, and Z. Bonaventura, “Electric field determination in air plasmas from intensity ratio of nitrogen spectral bands: I. Sensitivity analysis and uncertainty quantification of dominant processes,” *Plasma Sources Science and Technology* **27**, 085013 (2018), publisher: IOP Publishing.
 - ⁴³H. G. Weller, G. Tabor, H. Jasak, and C. Fureby, “A tensorial approach to computational continuum mechanics using object-oriented techniques,” *Computer in Physics* **12**, 620–631 (1998).
 - ⁴⁴G. Urdaneta, J. Bak, S. Pokharel, A. Tropina, R. B. Miles, and A. Dogariu, “Implementation of Laser Thomson Scattering for Femtosecond Laser-Generated Plasma Channel Characterization,” in *AIAA SCITECH 2024 Forum* (American Institute of Aeronautics and Astronautics, Orlando, FL, 2024).
 - ⁴⁵S. Pokharel, A. Dogariu, R. Miles, and A. Tropina, “Refractive Index Modification Induced by Femtosecond Laser Filament,” in *AIAA SCITECH 2024 Forum* (American Institute of Aeronautics and Astronautics, Orlando, FL, 2024).
 - ⁴⁶Y. Zhang, N. Calvert, M. N. Shneider, and R. B. Miles, “Enhancement of FLEET in Argon Gas Mixtures,” in *32nd AIAA Aerodynamic Measurement Technology and Ground Testing Conference* (American Institute of Aeronautics and Astronautics, Washington, D.C., 2016).
 - ⁴⁷S. B. Leonov, A. A. Firsov, M. A. Shurupov, J. B. Michael, M. N. Shneider, R. B. Miles, and N. A. Popov, “Femtosecond laser guiding of a high-voltage discharge and the restoration of dielectric strength in air and nitrogen,” *Physics of Plasmas* **19**, 123502 (2012).
 - ⁴⁸A. V. Volynets, D. V. Lopaev, T. V. Rakhimova, A. A. Chukalovsky, Y. A. Mankelevich, N. A. Popov, A. I. Zotovich, and A. T. Rakhimov, “N₂ dissociation and kinetics of N(4S) atoms in nitrogen DC glow discharge,” *Journal of Physics D: Applied Physics* **51**, 364002 (2018), publisher: IOP Publishing.
 - ⁴⁹M. N. Shneider, A. M. Zheltikov, and R. B. Miles, “Tailoring the air plasma with a double laser pulse,” *Physics of Plasmas* **18**, 063509 (2011).
 - ⁵⁰N. A. Popov, “Fast gas heating in a nitrogen–oxygen discharge plasma: I. Kinetic mechanism,” *Journal of Physics D: Applied Physics* **44**, 285201 (2011).
 - ⁵¹S. Pancheshnyi, B. Eismann, G. Hagelaar, and L. Pitchford, “ZDPlasKin: a new tool for plasmachemical simulations,” *Bulletin of the American Physical Society* (2008).
 - ⁵²J. Troe, “Temperature and pressure dependence of ion-molecule association and dissociation reactions: the N₂(+) + N₂ (+ M) ↔ N₄⁺ (+ M) reaction,” *Physical chemistry chemical physics: PCCP* **7**, 1560–1567 (2005).
 - ⁵³A. A. Ilyin, K. A. Shmirko, S. S. Golik, and D. Y. Proshchenko, “Emission of Nitrogen Molecules at Tight Focusing of Femtosecond Laser Pulses in Air,” *Russian Physics Journal* **64**, 1629–1636 (2022).
 - ⁵⁴C. Park, “Rate Parameters for Electronic Excitation of Diatomic Molecules 1. Electron-Impact Processes,” in *46th AIAA Aerospace Sciences Meeting and Exhibit, Aerospace Sciences Meetings* (American Institute of Aeronautics and Astronautics, 2008).
 - ⁵⁵Q. Niu, Z. Yuan, S. Dong, and H. Tan, “Assessment of nonequilibrium air-chemistry models on species formation in hypersonic shock layer,” *International Journal of Heat and Mass Transfer* **127**, 703–716 (2018).
 - ⁵⁶J. G. Kim and S. M. Jo, “Modification of chemical-kinetic parameters for 11-air species in re-entry flows,” *International Journal of Heat and Mass Transfer* **169**, 120950 (2021).
 - ⁵⁷M. S. Bak and M. A. Cappelli, “A Reduced Set of Air Plasma Reactions for Nanosecond Pulsed Plasmas,” *IEEE Transactions on Plasma Science* **43**, 995–1001 (2015), conference Name: IEEE Transactions on Plasma Science.
 - ⁵⁸J. Poggie, I. Adamovich, N. Bisek, and M. Nishihara, “Numerical simulation of nanosecond-pulse electrical discharges,” *Plasma Sources Science and Technology* **22**, 015001 (2012), publisher: IOP Publishing.
 - ⁵⁹I. M. Campbell, B. A. N. Thrush, and J. W. Linnett, “The recombination of nitrogen atoms and the nitrogen afterglow,” *Proceedings of the Royal Society of London. Series A. Mathematical and Physical Sciences* **296**, 201–221 (1997), publisher: Royal Society.
 - ⁶⁰S. Bodrov, N. Aleksandrov, M. Tsarev, A. Murzanev, I. Kochetov, and A. Stepanov, “Effect of an electric field on air filament decay at the trail of an intense femtosecond laser pulse,” *Physical Review E* **87**, 053101 (2013).
 - ⁶¹A. I. Florescu-Mitchell and J. B. A. Mitchell, “Dissociative recombination,” *Physics Reports* **430**, 277–374 (2006).
 - ⁶²“SIGLO Database,” <https://nl.lxcat.net>.
 - ⁶³P. Cicman, M. Francis, J. Skalny, S. Matejčík, and T. Märk, “The Rate Constant for Dissociative Electron Attachment to Ozone Revisited,” *Czechoslovak Journal of Physics* **53**, 181–190 (2003).
 - ⁶⁴G. J. M. Hagelaar and L. C. Pitchford, “Solving the Boltzmann equation to obtain electron transport coefficients and rate coefficients for fluid models,” *Plasma Sources Science and Technology* **14**, 722–733 (2005).
 - ⁶⁵“Explosion Dynamics Laboratory,” <https://shepherd.caltech.edu/EDL/PublicResources/sdt/thermo.html>. (),

- ⁶⁶“NIST WebBook,” (), <https://webbook.nist.gov/>: National Institute of Standards and Technology.
- ⁶⁷T. Hazenberg, J. F. J. Janssen, J. van Dijk, and J. A. van Oijen, “Consistent thermodynamics for plasma-assisted combustion,” *Proceedings of the Combustion Institute* **39**, 5541–5549 (2023).
- ⁶⁸“SIGLO Database,” (), <https://nl.lxcat.net>.
- ⁶⁹H. Böhlinger, D. W. Fahey, W. Lindinger, F. Howorka, F. C. Fehsenfeld, and D. L. Albritton, “Mobilities of several mass-identified positive and negative ions in air,” *International Journal of Mass Spectrometry and Ion Processes* **81**, 45–65 (1987).
- ⁷⁰H. W. Ellis, R. Y. Pai, E. W. McDaniel, E. A. Mason, and L. A. Viehland, “Transport properties of gaseous ions over a wide energy range,” *Atomic Data and Nuclear Data Tables* **17**, 177–210 (1976).
- ⁷¹A. F. Kennedy, Lawrence A., *Plasma Physics and Engineering*, 3rd ed. (CRC Press, Boca Raton, 2021).
- ⁷²C. Park, “Review of chemical-kinetic problems of future NASA missions. I - Earth entries,” *Journal of Thermophysics and Heat Transfer* **7**, 385–398 (1993).
- ⁷³D. O. Gericke, M. S. Murillo, and M. Schlanges, “Dense plasma temperature equilibration in the binary collision approximation,” *Physical Review E* **65**, 036418 (2002), publisher: American Physical Society.
- ⁷⁴Y. B. Zel’dovich and Y. P. Raizer, *Physics of Shock Waves and High-Temperature Hydrodynamic Phenomena* (Courier Corporation, 2002) google-Books-ID: jeIoAwAAQBAJ.
- ⁷⁵I. P. I. P. Raizer, *Gas discharge physics* (Springer, 1997).
- ⁷⁶D. S. Burch, S. J. Smith, and L. M. Branscomb, “Photodetachment of O_2^- ,” *Physical Review* **112**, 171–175 (1958), publisher: American Physical Society.
- ⁷⁷L. V. Keldysh, “IONIZATION IN THE FIELD OF A STRONG ELECTROMAGNETIC WAVE,” *Zh. Eksperim. i Teor. Fiz.* **Vol: 47** (1964), institution: Lebedev Inst. of Physics, Moscow.
- ⁷⁸J. Kasparian, R. Sauerbrey, and S. Chin, “The critical laser intensity of self-guided light filaments in air,” *Applied Physics B* **71**, 877–879 (2000).
- ⁷⁹M. Born and E. Wolf, *Principles of Optics*, 7th ed. (Cambridge University Press, 1999).
- ⁸⁰H. Zhao, “A fast sweeping method for Eikonal equations,” *Mathematics of Computation* **74**, 603–627 (2005).
- ⁸¹F. Théberge, W. Liu, P. T. Simard, A. Becker, and S. L. Chin, “Plasma density inside a femtosecond laser filament in air: Strong dependence on external focusing,” *Physical Review E - Statistical, Nonlinear, and Soft Matter Physics* **74**, 036406 (2006).
- ⁸²Y. Nakagawa, T. Yoshii, and F. Tochikubo, “Time evolution of atomic nitrogen density in pure-nitrogen-pulsed barrier discharge at sub-atmospheric pressure,” *Journal of Applied Physics* **131**, 113304 (2022).
- ⁸³S. Pokharel, R. Miles, and A. Tropina, “Refractive Index Modification and Plasma Characteristics of a Femtosecond Laser-Induced Filament in Nitrogen,” *IOP Journal of Physics D: Applied Physics*, Submitted, Under Review (2025).
- ⁸⁴J. Bak, S. Pokharel, C. Grunbok, G. U. Rincon, H. Hadden, A. Tropina, A. Dogariu, and R. B. Miles, “Characteristics of Plasma Decay in Dual Pulse Energy Deposition for Air and Nitrogen in Atmospheric Pressure,” in *AIAA AVIATION FORUM AND ASCEND 2024* (American Institute of Aeronautics and Astronautics, 2024).
- ⁸⁵S. Pokharel, J. Bak, A. Tropina, and R. B. Miles, “Plasma Enhancement of fs-Filament in N₂-O₂ Mixture With ns-Heating Pulse,” in *AIAA SCITECH 2025 Forum* (American Institute of Aeronautics and Astronautics, 2025).